# CHAPTER-4

# VALIDATION OF NUMERICAL & EXPERIMENTAL WORK

## 4.1 VALIDATION OF CAVITATION

In the present study, the commercial CFD code ANSYS-Fluent is used to identify appropriate numerical models which can simulate the cavitation flow more accurately at a low computational cost. A systematic study has been carried out for cavitation flow. The nozzle geometry and boundary conditions are identical to Winklhofer et al. [14] experimental work. The simulation has been carried out with k-ε RNG, k- ε REALIZABLE, and k-ω SST turbulent model. The SS and ZGB cavitation models are compared based on the vapor volume fraction. Finally, the mixture and the VOF multiphase model are used with dispersed and sharp interface capture options. The best-suited numerical model configuration has been suggested based on the above study.

### 4.1.1 Winklhofer throttle geometry

Qualitative information in a real-size nozzle is essential to understanding cavitation flow and its complete behavior. However, direct observation of cavitation flow in the real condition is difficult due to very small space and time parameters. To observe cavitation in a real-size nozzle, it must be transparent and capable of withstanding high injection pressure and choking condition. A good quality cavitation image will be convenient for the reader and model validation. Winklhofer et al. [14] experimented with a real-sized two-dimensional throttle (transparent rectangular cross-section) working with European diesel fuel, as shown in Fig.4.1. Optical methods were developed and applied to diagnose high-pressure diesel flow at transient conditions using interferometry imaging shown in Fig. 4.2. They use three different nozzles named J, U, and W throttle with different outlet contractions, i.e., 0 %, 5 % & 10 %, respectively.

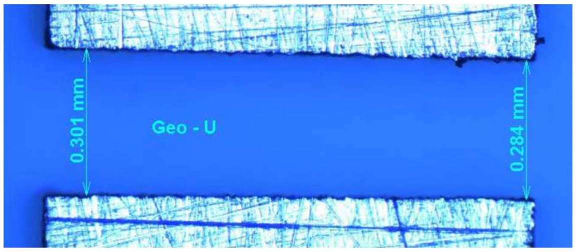

**Fig. 4.1** Two-dimensional throttle (transparent rectangular cross-section) geometry [14]

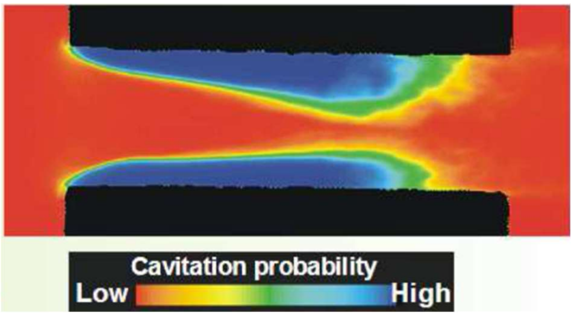

**Fig. 4.2** Cavitation field capture using interferometry imaging technique [14]

They measured values of the mass flow rate of diesel at different pressure drops and predicted cavitation inception and choking conditions. In the present study, identical geometry & boundary condition has been used to analyse the cavitation flow inside the nozzle as shown in Fig. 4.3. The fuel properties considered similar to Winklhofer et al. [14]data. The density of diesel's liquid and vapor phases are 830 kg/m$^3$ and 9.4 kg/m$^3$, respectively. The viscosity of liquid and vapor phases are considered as 0.00336 kg/ms and 7.006 x 10$^{-6}$ kg/ms, respectively.

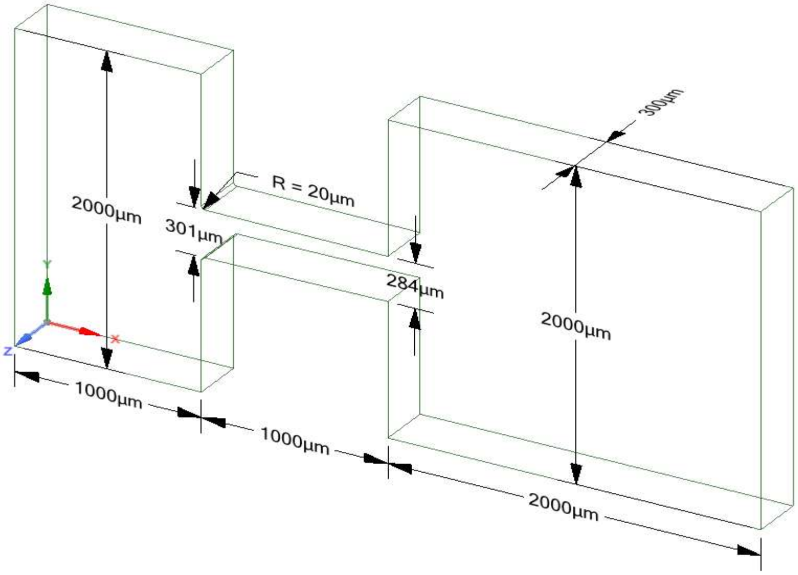

**Fig. 4.3** Computational domain with its dimension

### 4.1.2 Grid Generation

The computational domain was discretized using a cut-cell method with structural hexahedral mesh elements. The specific mesh refinement treatment has been performed near the nozzle inlet corner, as shown in Fig. 4.4. The results of the CFD simulation depend on the computational grid quality and size. Therefore, it is important to resolve the grid to the extent that the solution becomes independent of the grid size. However, there is a balance required between grid refinement and computational cost. The grid independence test has been performed and the results of the mass flow rate of fuel are shown in Fig.4.5. It is observed that the variation in the calculated mass flow rate is least with 299324 elements. Further refinement in the mesh would not affect the orthogonal quality and aspect ratio of the grid. Hence considering the best compromise between the consistency of results & computational cost, 299324 mesh elements have been chosen for the further simulation study.

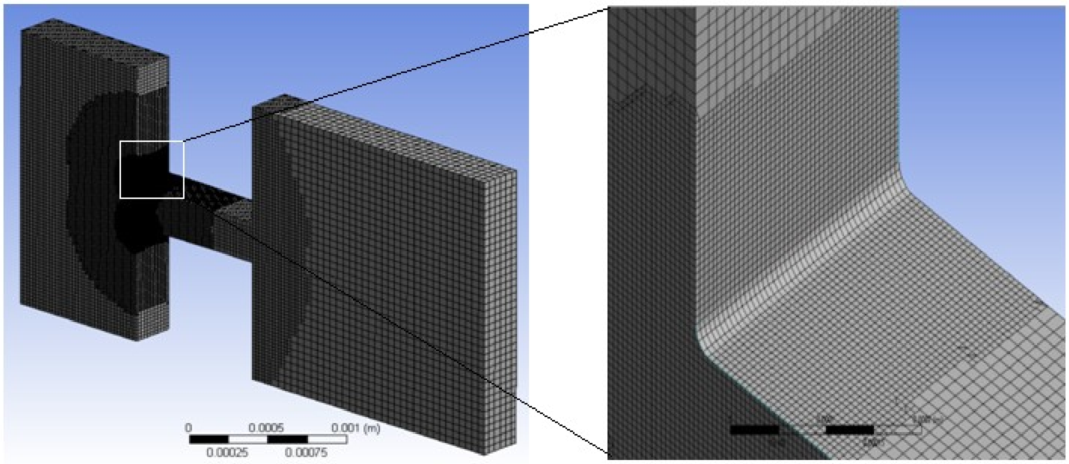

**Fig. 4.4** Grid generation with refinement at throttle inlet

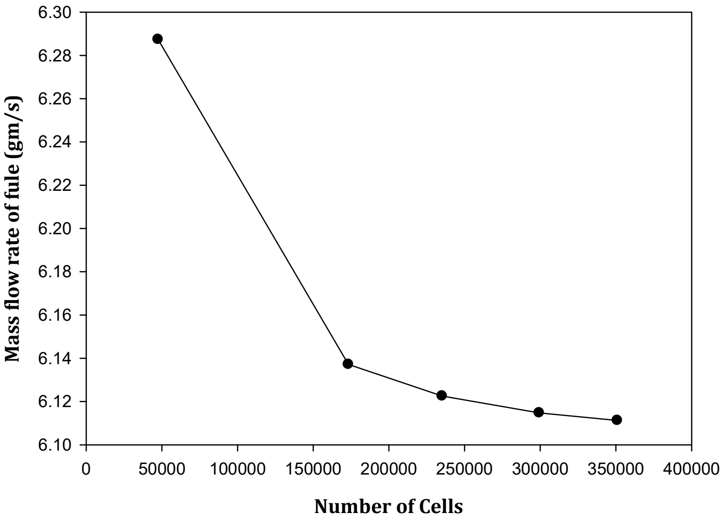

**Fig. 4.5** Effect of number of mesh elements on the mass flow rate of fuel

### 4.1.3 Numerical set-up

The fuel is injected at a constant pressure of 100 bar and varied the outlet pressure from 15 bar to 80 bar. No-slip boundary condition has been employed to the wall. The turbulence intensity and hydraulic diameter are defined at the inlet and outlet of the nozzle. The finite volume approach has been used with commercial CFD software ANSYS-Fluent. The pressure-based segregated algorithm has been used to solve the governing equation. The pressure-velocity coupling has been solved by the Coupled algorithm. The special discretization of the pressure is done by using PRESTO! method. The second-order upwind scheme is used for the momentum equation. The volume fraction and turbulent kinetic energy are discretised by the first-order upwind scheme. During the transient simulation, the Corant number is set as 0.25 with minimum and maximum time step sizes of $10^{-8}$ sec to $10^{-6}$ sec respectively. The convergence criteria for the governing equation are set to $10^{-6}$. The under-relaxation factor has been adjusted (between 0 and 1) to ensure the solution's stability. The Courant number, also known as the CFL (Courant-Friedrichs-Lewy) number, is a dimensionless number that is critical in numerical simulations of time-dependent problems, such as those solved with the Volume of Fluid (VOF) model in ANSYS Fluent. The Courant number ensures numerical stability and accuracy in transient flow solutions. The Courant number is defined as:

$$CFL = \frac{U\Delta t}{\Delta x} < 1 \tag{4.1}$$

Where U is the local velocity, Δt is the time step size and Δx is the grid size. A Courant number less than 1 ensures that the fluid interface is accurately tracked and that the simulation remains stable.

### 4.1.4 Initial Validation

To validate this numerical setup, comparisons were made between the results of simulations and that of an actual experiment by Winklhofer et al. [14] quantitative &qualitative validation have been shown in Fig. 4.6, 4.7 &4.8. A range of pressure differences has been used to calculate the mass flow rate of fuel.

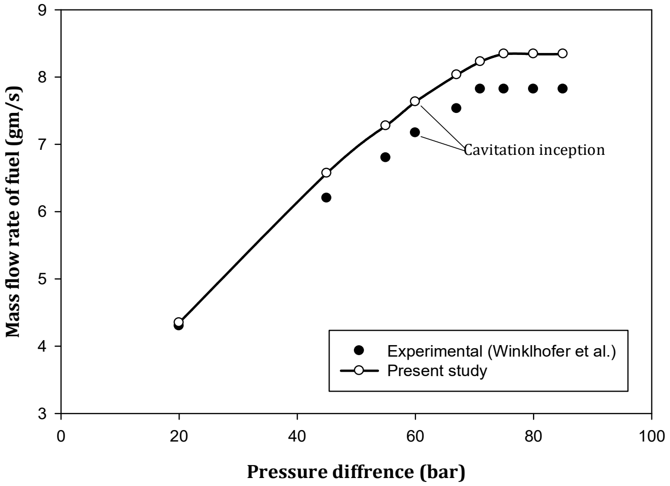

**Fig. 4.6** Quantitative comparison of fuel mass flow rate with experimental results

Present results show good agreement with the experimental data of Winklhofer et al. [14] with a maximum error of 7% as shown in Fig. 4.6. It can be attributed to the assumptions taken in simulations and material properties variations. But simulation results hold a good trend following experimental results. Fig. 4.7 shows the velocity profile at a 53 μm distance from the inlet of the nozzle for the pressure difference of 67 bar & 85 bar, which are compared with experimental data. This study observes mass flow rate calculated is higher than the experimental claim, which results in the velocity profile being over-predict for both cases. In the experimental images, the red colour indicates the liquid fraction and blue colour used for the vapor; a similar colour map is used for validation purposes, as shown in Fig.4.8.

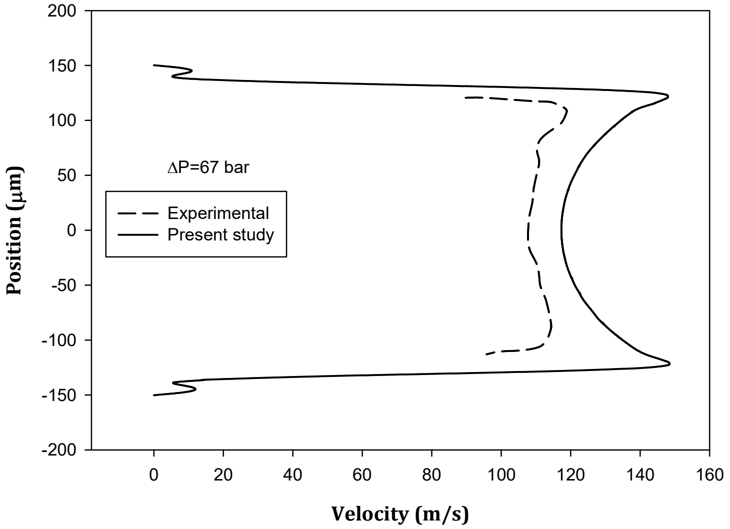

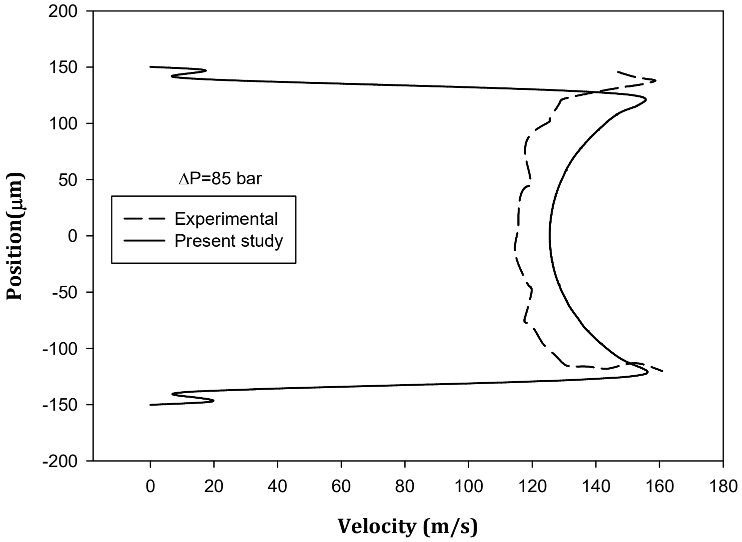

**Fig. 4.7** Comparison of the velocity profiles at 53 μm from the nozzle inlet

It is observed that the numerical model accurately predicts the inception of cavitation, although, with a large pressure difference, it under predicts the extent of the cavitation zone. The results obtained in the experimental work are the integrated effect of the light transmitted through the two-phase flow. However, the current results belong to a single plane in the fluid domain.

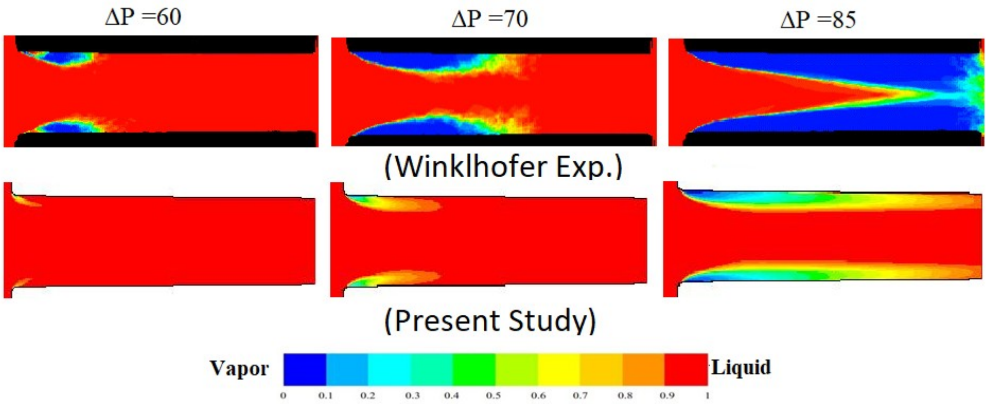

**Fig.4.8** Qualitative comparison of Liquid volume fraction with experimental results [14]

### 4.1.5 Assessment of Turbulence model

There are three turbulence models, i.e., (1) k-ε RNG (Renormalization Group), (2) k-ε REALIZABLE (3) k-ω SST (Shear Stress Transport), which have been tested to capture cavitation and compared with available experimental results. The k-ε model is more suitable for the shear-free region; however, k-ω provides a more accurate solution near the wall region. In the k- ω SST model, the features of both k-ε and k-ω are integrated, which automatically activates k-ε and k-ω over the domain. Therefore, the k-ω SST model is likely to perform well in the near-wall zone.

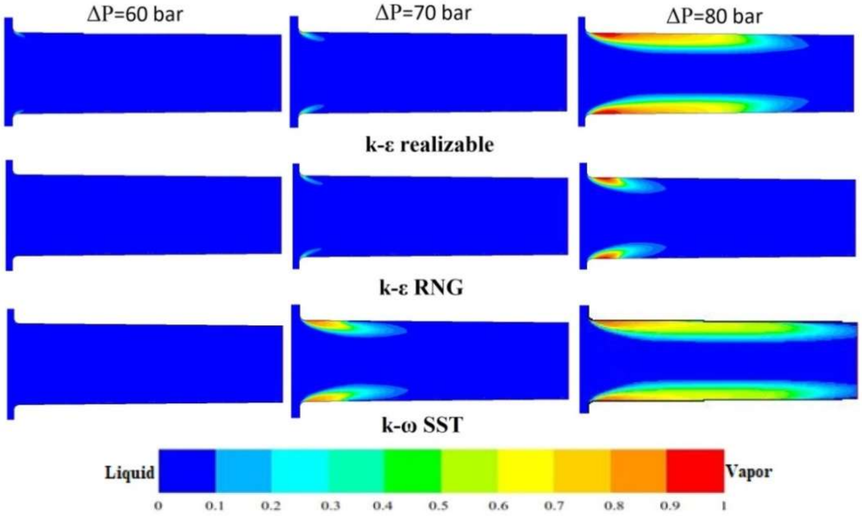

**Fig. 4.9** Volume fraction of vapor at with different of turbulence model

The recirculation and shear zone will increase with a pressure drop at the nozzle entry. The k-ε RNG, k-ε realizable turbulence model performs weakly in the shear zone and under predicts the cavitation intensity shown in Fig. 4.9. It is observed that results with the k-ω SST turbulent model show consistency with experimental results. It is also reasonably good with a wide range of flows. The mass flow rate of fuel has been calculated at variable pressure conditions and compared with experimental data as shown in Fig.4.10. The nozzle's choking is indicated only with the k-ω SST model; other turbulence models fail to determine choking. It is concluded that the k-ω SST model is preferred to simulate cavitation flow and is used in further simulation work.

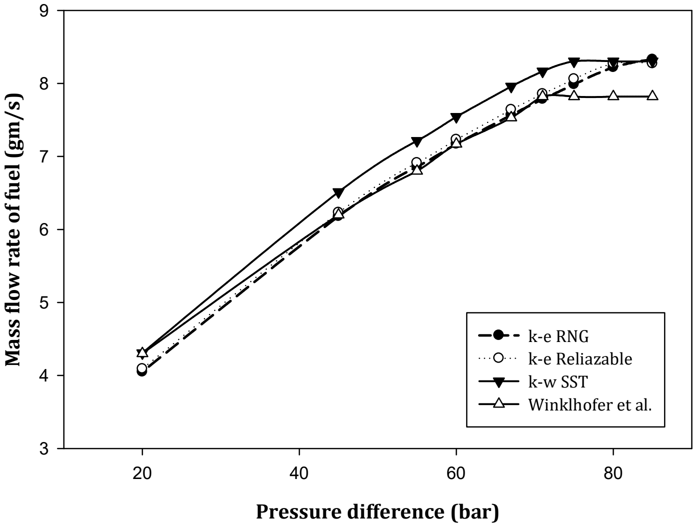

**Fig. 4.10** Comparision of turbulence model based on the mass flow rate of fuel

### 4.1.6 Assessment of Cavitation Model

The two cavitation models i.e., (1) the SS (Schnerr and Sauer) model and (2) the ZGB (Zwart-Gerber-Belamri) model, are compared. It has been seen through the results that the SS cavitation model is inaccurate as it fails to capture cavitation inception at a pressure difference of 60 bar. The methodology adopted for the source term formulation leads to the poor performance of the SS model. In the SS model, the bubble density per unit volume of liquid ($n_B$) is to be considered at $10^{-13}$ for the best result. The ZGB contains many tuning parameters that provide better results. The higher initial vaporization constant in the ZGB model gives a higher vapor fraction as compared to the SS model. The evaporation and condensation rates in the ZGB model are linear, however, in the SS model, they are non-linear. With the ZGB model, cavitation inception appears at a pressure difference of 60 bar, which supports the experimental data shown in Fig. 4.11. The SS cavitation model over-predicts the mass flow rate of fuel over the range of pressure differences, as shown in Fig. 4.12. This is expected since the SS model under predicts the cavitation region at a higher-pressure difference. However, the ZGB model exhibits good qualitative and quantitative results with experimental data. Based on this study, it is concluded that the ZGB is a preferred cavitation model.

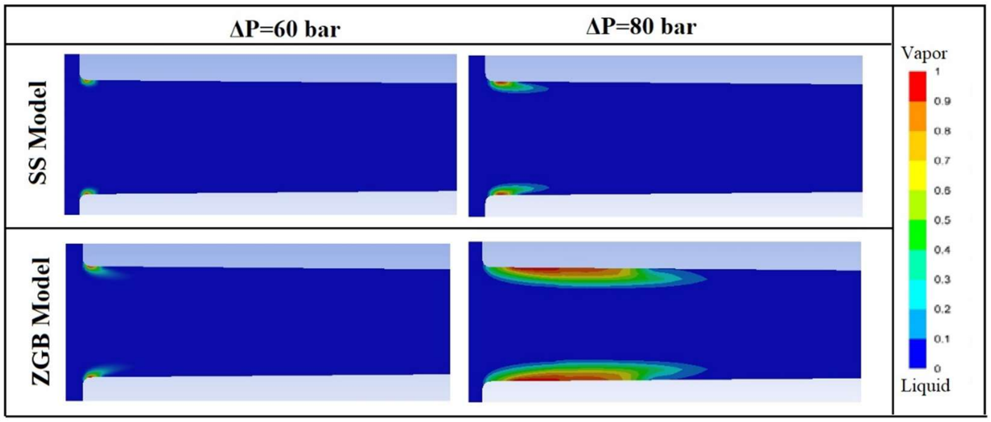

**Fig. 4. 11** Comparison of the SS and the ZGB cavitation model based on the volume fraction of vapor

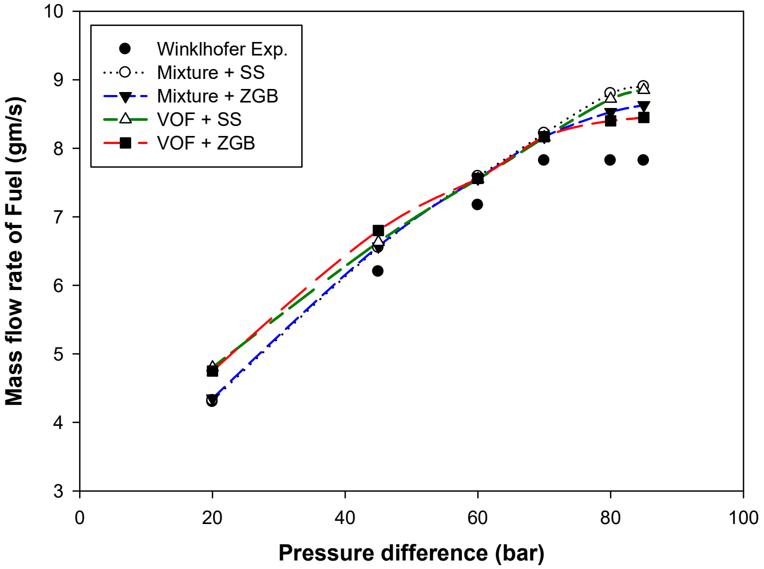

**Fig. 4. 12** Comparison of the predicted mass flow rate with the Mixture and VOF multiphase model in the SS & ZGB cavitation model combination at different pressure differentials

### 4.1.7 Assessment of Multi-phase model & Interface modelling

The volume of fluid (VOF) is a surface tracking model designed for two immiscible fluids where the interface is required to capture. The mixture model differs from the VOF model in two aspects. (i) The mixture model allows for the movement of the phases with different velocities by considering the concept of slip velocity. (ii) The mixture model also allows the interpenetrating of mass, momentum, and energy between the phases. The mixture and VOF multiphase model have been used in conjunction with the SS and ZGB cavitation models. The simulation has been carried out to calculate the fuel mass flow rate at variable pressure differences and compared with Winklhofer et al. [14] experimental results. The mass flow rate prediction by the ZGB cavitation model with both the mixture and VOF is closer to experimental data; than that with the SS cavitation model. Particularly, at the higher-pressure difference, the VOF with the ZGB precisely predicts the trend of choked flow. Although the SS cavitation model fails to predict chocking, mass flow rate increases continuously with pressure for both the mixture and the VOF model. No significant difference was observed in the qualitative comparison of cavitation flow with the mixture and VOF models. In extension, the dispersed and sharp interface approach with the mixture and VOF model is implemented in ANSYS-Fluent. Comparisons between the predictions from the two models' mixture and VOF (with different inter-phase approaches) are shown in Fig.4.13. The mixture model works better with the dispersed option and does not show a major difference with the sharp interface option. The VOF model will better capture the interface for a given mesh resolution as shown in Fig 4.13 (d). It is observed that the overall structure of cavitation is well captured with both models. Although, the smaller structures like bubble formation and ligament breakup are only captured with the VOF sharp interface option. This is due to consideration of the effect of surface tension in the VOF model.

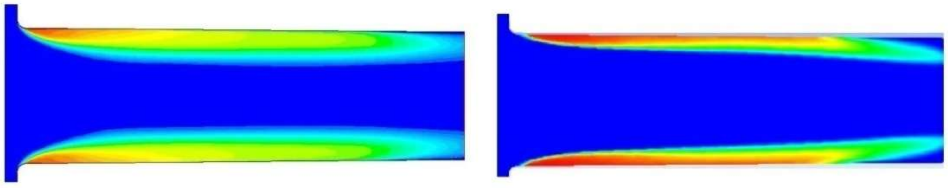

**(a) Mixture model with Dispersed interface** **(b) Mixture model with Sharp interface**

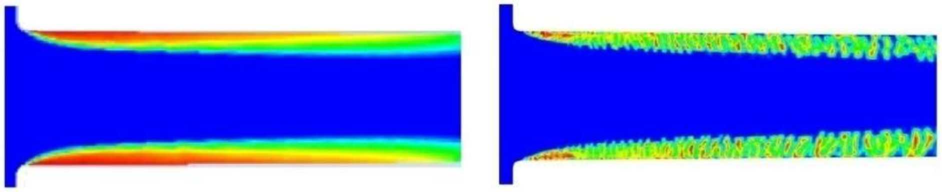

**(c) VOF model with Dispersed interface** **(d) VOF model with Sharp interface**

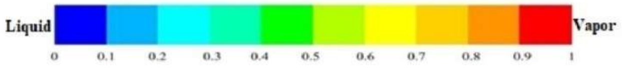

**Fig. 4.13** Comparison of vapor fraction contour between the mixture and VOF model in conjunction with dispersed and sharp interface option at ΔP=85 bar.

### 4.1.8 Summary of numerical modelling of cavitation flow

The accuracy of the numerical solution depends on the appropriate section model and sub-model. The main idea behind this work is to identify the best-suited numerical model for the cavitation flow. The proposed model must be accurate & computationally less costly. The cavitation phenomenon involved gas-liquid flow which is turbulent. A systematic study has been carried out with three different turbulence models, two cavitations models and two multiphase models. The results of the mass flow rate of fuel were compared to experimental data. Typically, all combinations overstate the mass flow rate to experimental data. The simulation results calculate the mass flow rate based on the nozzle's exit area. However, the reduction in the effective area during the cavitation flow is not considered using CFD calculation. This is why all models projected a higher mass flow rate than the actual mass flow rate.

The maximum error with different combinations of the model has been calculated and reported in Fig.4.14. The combination of the VOF+ZGB+ k-ω SST exhibits the least error among all cases. Moreover, LES based turbulence model is widely adopted to capture the detail of bubble and ligament formation. In the present work, the VOF is tuned with a sharp interface capturing method using the k-ω SST turbulence model. The present method required substantially low computational time (60 clock hours with 4GB RAM) as compared to the similar work reported by S. Rojas et al. [52] (250 clock hour with 64 GB RAM) using large eddy simulation (LES).

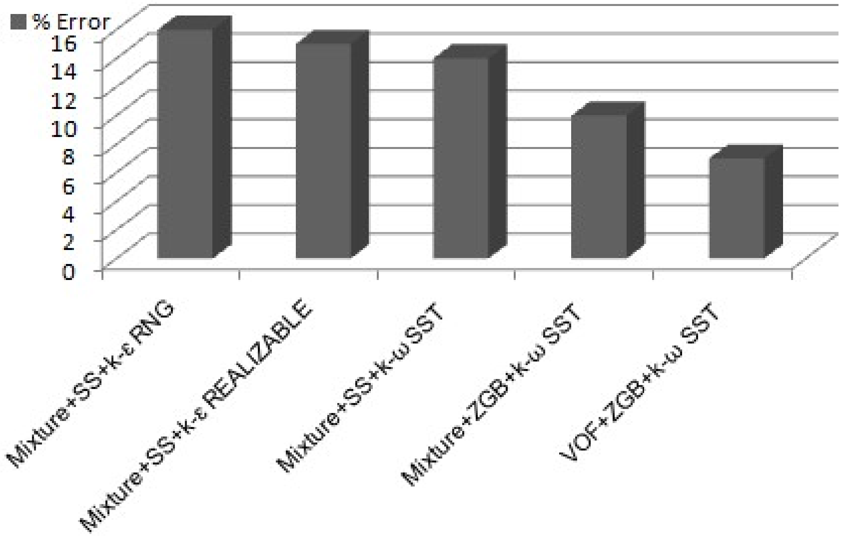

**Fig.4.14** Percentage error mass flow rate of the fuel with different combinations of numerical models

### 4.1.9 Transient Simulation

The cavitation flows involved continuous bubble growth and collapse; they also travelled toward the outlet of the nozzle. Such phenomena must be solved using a time-dependent formulation. The transient simulation has been carried out with a pressure difference of 85 bar. The time step during the simulation is kept at $10^{-7}$ s with the VOF+ZGB model with a sharp interface option. The mechanism of bubble formation and its movement inside the nozzle is shown in Fig. 4.15. The inception of cavitation begins after 10µs at the round corner of the throttle inlet. As time proceeds, the cavitation region moves downstream and fully develops up to 100 µs. The bubble breakup and ligament formation are visible in the vapor fraction contour. The results obtained at the throttle outlet predict the fuel's primary breakup. This is very useful information for coupling inner nozzle flow and spray formation.

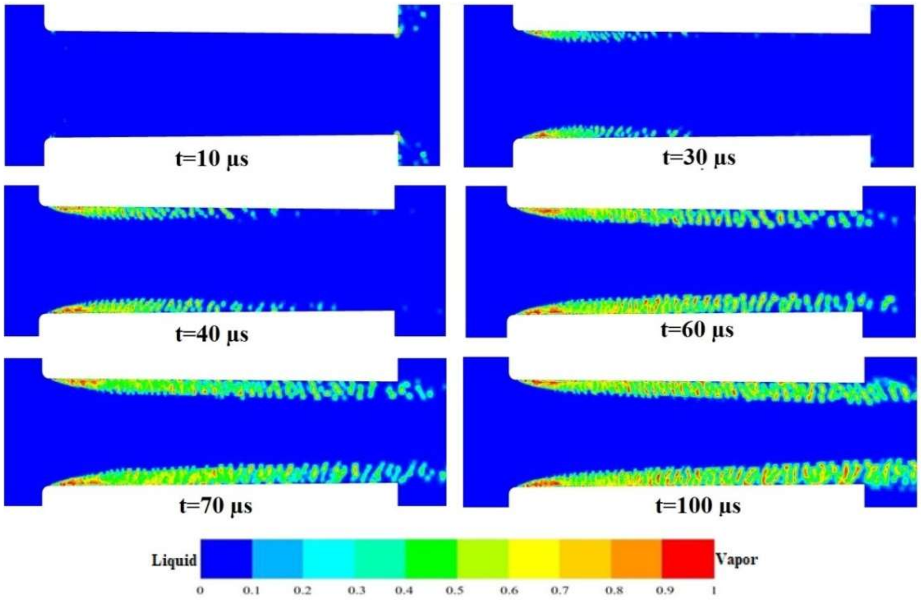

**Fig. 4.15** Vapour bubble formation and its development inside the throttle at ΔP=85 bar

## 4.2 VALIDATION OF SPRAY

In the present section, ANSYS-FLUENT was employed to study non-evaporating spray. FLUENT provides a discrete phase model (DPM) to simulate spray characteristics, which is based on the Lagrangian drop Eulerian fluid method. It allows for tracking the fuel droplets (discrete phase) in the Lagrangian frame of reference and the continuous gas phase in the Eulerian frame of reference. Furthermore, the spray breakup models have been used & compared to capture droplet breakup phenomena. When the fuel droplets travel in the chamber, they experience the turbulent vortex, which causes the motion of the particles to shift from straight lines to non-smooth curves. The interaction between the droplet and discrete vortex is taken into account by the discrete random walk (DRW) model. The discrete random walk model was used to simulate the turbulent diffusion of the spray droplets.

### 4.2.1 Computational domain & Boundary condition

The computational geometry used for the present study is based on a single-hole injector experimentally studied by Wang et al. [105]. For validation purposes nozzle with 0.16 mm diameter and 1 mm in length is used to inject the diesel at the rate of 2.225 gm/s at 300 MPa injection pressure. The fuel injection chamber is symmetrical in shape; hence simulation is carried out with an axi-symmetric computational domain which is created in the ANSYS-Design modeller. The discretization of the domain is done with the use of ANSYS-ICEM, which allows the creation of fine structural mesh in the centre core of the chamber shown in Fig.4.16.

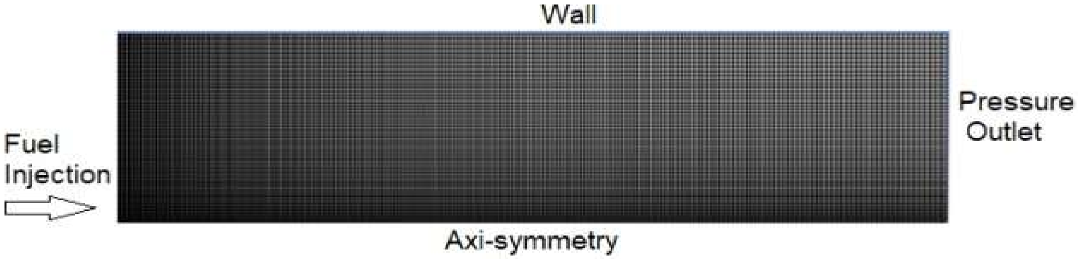

**Fig. 4.16** Boundary condition with detail mesh geometry

### 4.2.2 Effect of mesh size

The results obtained with the use of computational fluid dynamics always depend on mesh size. So, it is essential to refine the mesh, so that solution results are not dependent on mesh size. Moreover, sufficient grid size is essential to simulate discrete phase particles.

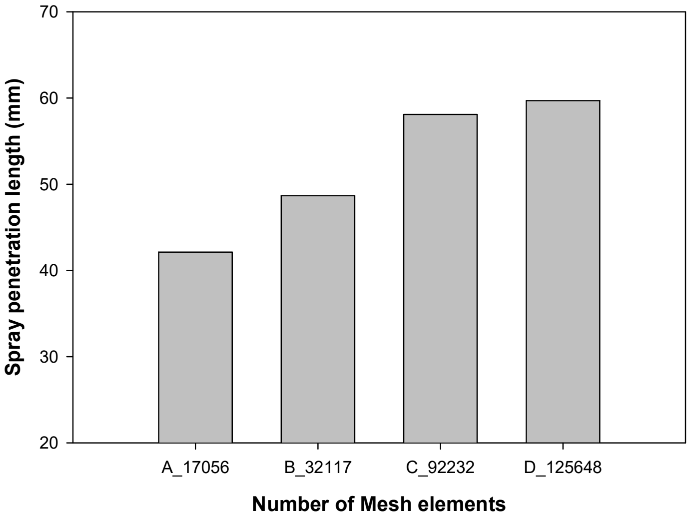

**Fig. 4.17** Effect of mesh elements on spray penetration length

Four different mesh sizes had been used to perform the grid independence study shown in Fig. 4.17. With the case, D total number of mesh elements is 125648 with a minimum element size of 1μm has been used for further study. The time step of $1 \times 10^{-6}$ seconds has been considered to avoid solution instability.

### 4.2.3 Effect of the Spray breakup model

The atomization of the fuel is a very complex phenomenon, which required a very expensive instrument to diagnostics of its spray characteristics, specifically with high injection pressure. Due to this reason very, little experimental research is available, which will provide inside detail of spray formation. In the present study, the spray breakup model has been validated with the experimental work carried out by Wang et al. [105]. For validation purposes nozzle with a 0.16 mm diameter is used to inject the diesel at the rate of 2.225 g/s at 300 MPa injection pressure. Most of the literature describes the spray tip penetration to study spray characteristics. Spray tip penetration can be defined as the farthest axial distance of the spray boundary from the nozzle tip. The spray tip penetration (STP) of the diesel spray at the different injection times has been calculated. The development of spray has been captured up to 1ms with the time interval of 0.1ms. Wang et al. [105] reported spray tip penetration at 0.7 ms as shown in Fig. 4.18.

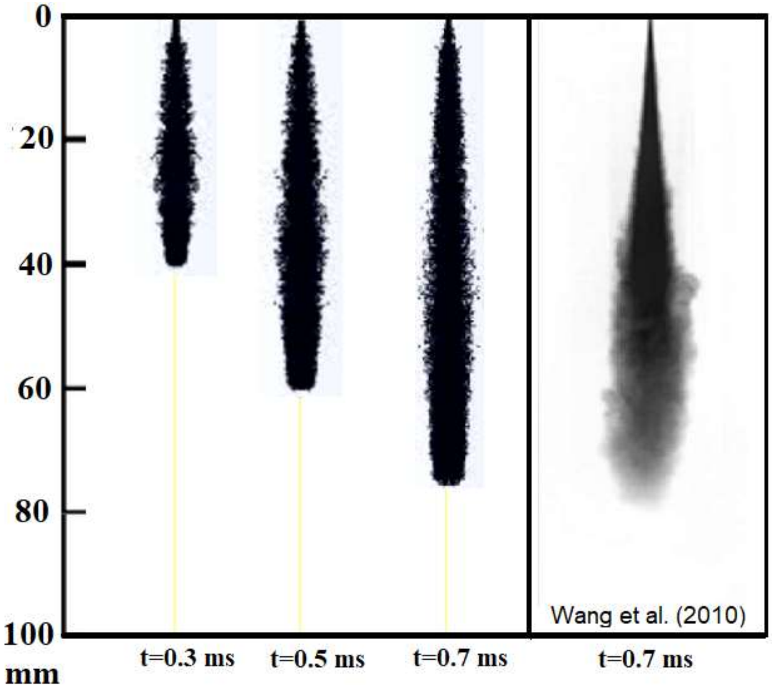

**Fig. 4.18** Spray developments compared with the experimental work

To compare the capability of different spray models, Single Size Distribution (SSD), Wave and the Kelvin-Helmholtz Rayleigh-Taylor (KHRT) models have been implemented.

The spray tip penetration grows more quickly in the beginning of the injection and less rapidly in the closing stages. The results obtained at the beginning of the fuel injection are quite reasonable with the experimental trend. The KHRT and the Wave model predict the penetration length reasonably good as compared to the SSD model shown in Fig. 4.19. Moreover, the spray shape obtained in the WAVE model is closer to the experimental work of Wang et al. [105].

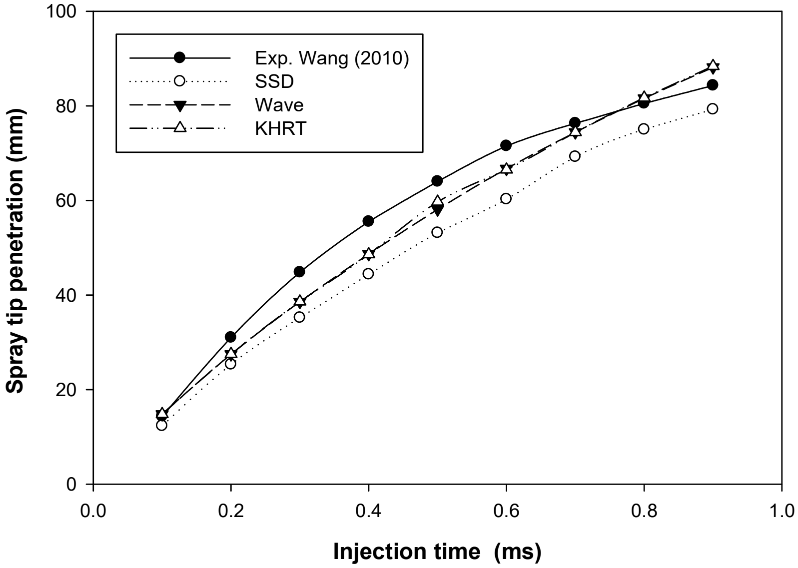

**Fig. 4.19** Comparison of Spray tip penetration of different spray breakup models with experimental data

Understanding and controlling droplet size metrics are crucial in designing efficient fuel injection systems. Achieving a spray with small minimum diameters, controlled maximum diameters, and an optimized Sauter mean diameter can lead to better fuel atomization, more efficient combustion, and reduced emissions. Table 4.1provides the particle summary of spray which injected at 300MPa.

**Table 4.1** Particle summary for Diesel

| Sauter mean diameter (SDM) | Max. particle diameter | Min. particle diameter |
|---|---|---|
| 6.73 µm | 57.75 µm | 0.101 µm |

## 4.3 VALIDATION OF TWO-STEP COUPLED METHOD

### 4.3.1 ECN Spray C Fuel Injector nozzle

The Engine Combustion Network (ECN) created the spray C fuel injector nozzle as part of the 4th generation of fuel injectors to investigate cavitation flow dynamics. This nozzle with a single cylindrical hole was designed to resemble practical fuel injectors with a relatively large orifice diameter (inlet) of 0.187 mm and minimal hydro erosion. The nozzle holes have a slightly diverging geometry to promote strong cavitation flow. The ECN (Engine Combustion Network) group obtained ten large-nozzles, single-hole diesel injectors from Bosch. These solenoid-activated injectors are designed for modern advanced injection systems, with a nominal pressure rating of 2200 bar and a capability of up to 2500 bar. The injectors feature an axial single-hole nozzle, which is intended to facilitate optical diagnostics of the fuel spray. Spray C diesel injector nozzles that have a nominal outlet diameter of 0.2 mm. The orifice of these nozzles is cylindrical, with a k-factor (orifice discharge coefficient) equal to zero. Additionally, the orifice has undergone 5% hydro-grinding, which has relatively smoothed the contours of the orifice. Table 4.2 describes the nominal specifications of the single hole injector.

**Table 4.2** Nominal specifications of ECN spray C injector

| Common rail fuel injector | Bosch 3-22 | Bosch 3-22 |
|---|---|---|
| Injector part serial number | 210037C | 210003C |
| Nominal diameter | 0.200 mm | 0.200 mm |
| Inlet diameter (actual) | 0.187 mm | 0.187 mm |
| Outlet diameter (actual) | 0.208 mm | 0.212 mm |
| Hole length | 1 mm | 1 mm |
| k-factor | 0 | 0 |
| Nozzle shaping | 5% hydro-erosion | 5% hydro-erosion |

The ECN is considered a domain with a fixed needle positioned at the highest upward point. The "Generation 2" measurements conducted at Argonne National Laboratory's Advanced Photon Source have a higher measurement resolution than prior commercial x-ray CT, and hence are used in the current study. Various surface (STL) files have been created based on these results, particularly for Injector 210037. Figure 4.20 depict X-ray computed tomography (CT) image of Injector 210037C. To simplify calculations, an axis-symmetric "wire frame" generated from Gen 2 geometry was used in current research work as shown in Fig. 4.21. In this study, we employed identical boundary conditions and fuel to ensure a direct comparison between our obtained results and the experimental data available from the Engine Combustion Network. Table 4.2 shows the boundary conditions for nozzle and spray simulation. This approach enhances the reliability and relevance of our findings by establishing a consistent and comparable basis for evaluation. Moreover, current method is also compared with similar method proposed by Payri R. et al. [109], Tahmasebi E. et al. [110].

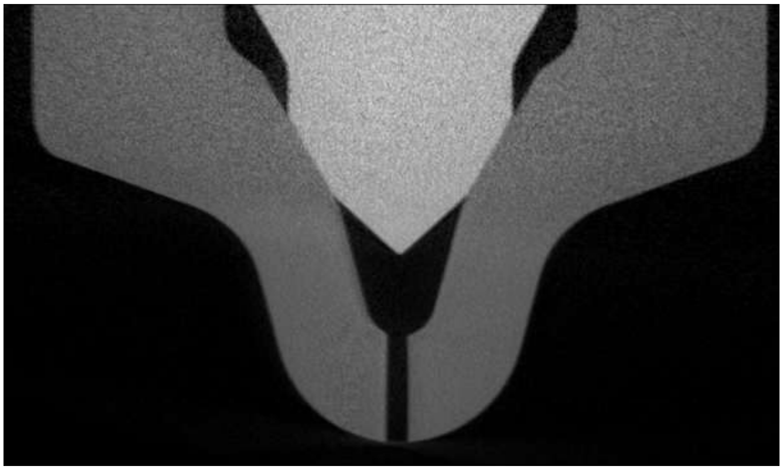

**Fig 4.20** X-ray CT image at the injector's central cross-section[106,107]

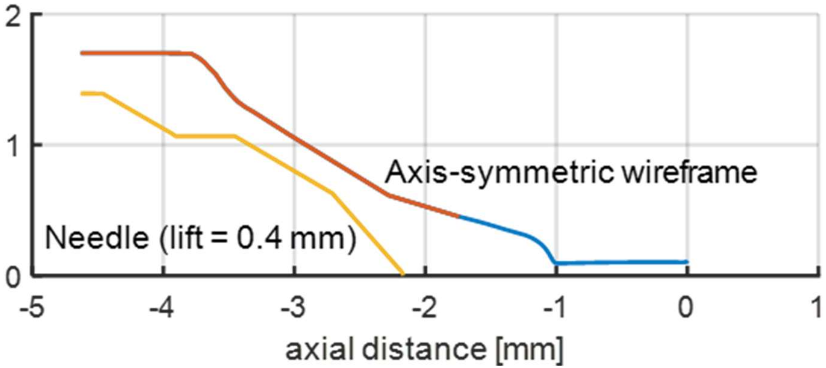

**Fig 4.21** Two-dimentional axis-symmetric wireframe geometry [106, 107]

### 4.3.2Geometry and Mesh for internal nozzle flow

A computational domain has been generated using ANSYS- Space Claim based on wireframe geometry provided by ECN. The model geometry was discretized using ANSYS meshing tool. For two-dimensional geometry two different types of mesh elements are available, i.e. quadrilateral and triangle. Quadrilateral mesh elements can provide good quality solutions as compare to triangle mesh elements. It has been divided into multiple faces to ensure high-quality mesh discretisation, and element costume sizes are provided using a cut-cell approach. A specific mesh refinement treatment near the nozzle edge has been performed and is shown in the Fig. 4.22.

A nozzle mesh sensitivity test is performed to determine the optimum number of cells in this model. For different numbers of elements, mass flow rates are calculated. Mesh element size and quality affect the results, and hence sufficient refinement must be provided to ensure the most reliable results, which do not depend on element size. Five different mesh sizes have been tested to evaluate the effect of mesh on the mass flow rate of diesel, as shown in Fig. 4.23.

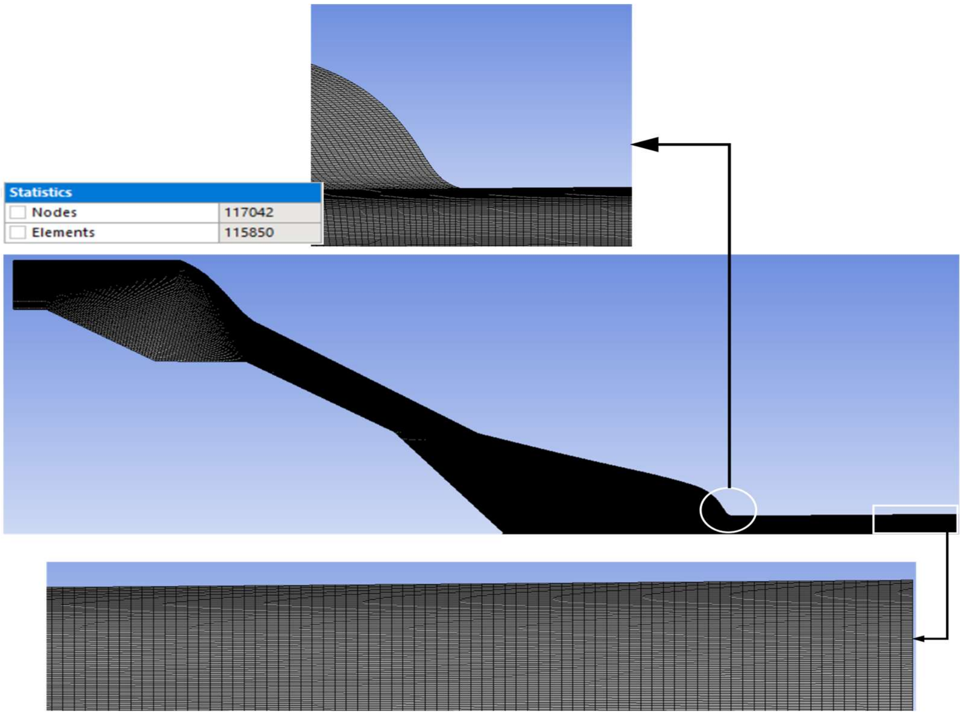

Statistics

Nodes 117042

Elements 115850

**Fig. 4.22** Mesh generation for internal flow

In this work, meshing is done with the help of the default meshing tool in the ANSYS. As in the proximity area of rounded corners, variations in parameters are very rapid due to the cavitation phenomenon. A refined mesh helps to get more accurate results. Fine mesh elements cause more accurate results, but at the same time, the time of calculation also increases. There is always some range of optimum numbers of elements, which gives a balance between the time of calculation and the accuracy of the results. A total 115850 number of cells are seen as most suited and adopted for further study.

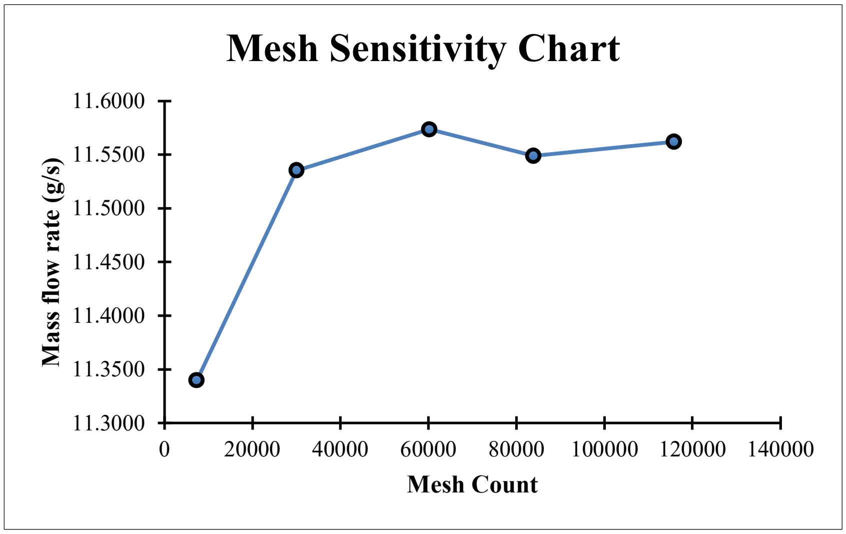

**Fig 4.23** Mesh sensitivity study for internal flow

### 4.3.3Geometry and Mesh for spray formation

We use a two-way coupling method for spray breakup, as was previously discussed. We use straightforward rectangular geometry for spray simulation. For meshing, we used edge sizing and quad element meshing with adequate bias and growth factor to have a finer mesh in the core region of the spray as well as at the inlet entry point of domain. Fig. 4.24 shows the spray simulation's geometry and mesh quality. A total 960000number of elements in this structured mesh were selected after performing a grid independence test with a minimum orthogonal quality of 1.

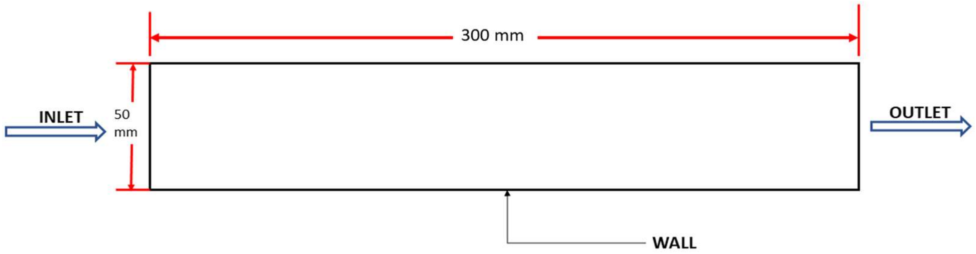

(a) Geometry for spray simulation

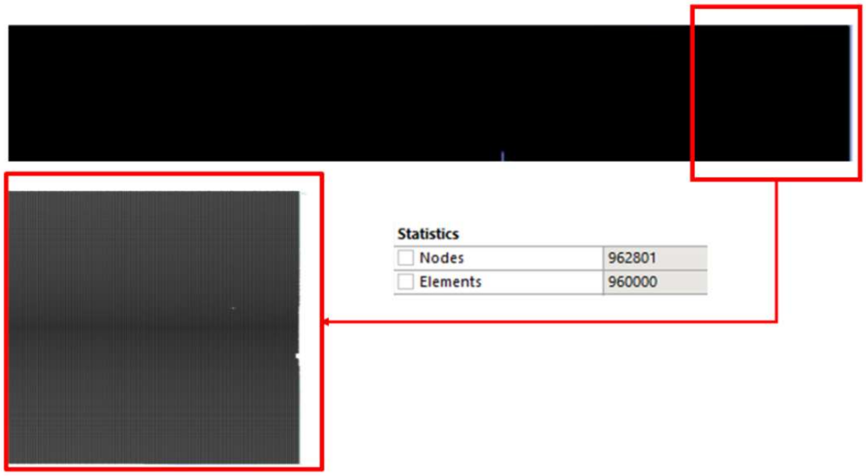

**Statistics**

| | |
|---|---|
| ☐ Nodes | 962801 |
| ☐ Elements | 960000 |

(b) Mesh quality for spray simulation

**Fig. 4.24** Geometry and mesh quality for spray simulation

This study uses the n-dodecane as working fuel as per the ECN guidelines for standard substitute for diesel. Its thermo-physical properties are obtained from National Institute of Standards and Technology (NIST) database, which are in concurrence with the investigations performed by R. Payriet al. [109] and Tahmasebi et al. [110]. Table 4.3 discusses the properties of n-dodecane for reference.

### 4.3.4Initial and boundary condition

When employing numerical methods, different boundary conditions may provide different results. Some of these might change the domain in a non-physical way. For physical stability inside the domain, it is crucial to set up appropriate boundary conditions.

**Table 4.3** Thermo physical properties of n-dodecane and diesel fuel

| | n-dodecane | diesel |
|---|---|---|
| Liquid saturation density (kg /m$^3$) | 697 | 830 |
| Vapor density (kg /m$^3$) | 0.16 | 0.1361 |
| Saturation pressure (Pa) | 2567 | 2000 |
| Liquid dynamic viscosity (Pa ·s) | 0.000836 | 0.001517 |
| Vapor dynamic viscosity (Pa ·s) | 5.44e-6 | 5.94E-06 |

The upstream situation in a fuel injector nozzle is the injection of high-pressure fluid inside the nozzle. We have used pressure inlet and pressure outlet boundary conditions for our problem. The no-slip condition is assigned at the wall boundary due to zero velocity. The solver's purpose is to model high-velocity flows in tiny fuel injector nozzles. The simulation ignores the fluid-solid wall contact since it has negligible viscous effects. A time-varying velocity condition is used to simulate the nozzle's inlet. The turbulent length scale is equal to 10% of the orifice outlet diameter, and the turbulent intensity at the intake is equal to 5% of the imposed velocity. The nozzle is initially thought to be filled with stagnant fuel (up to the orifice output). For the multiphase method, no-slip conditions are also assumed at the liquid-vapor interface. The computational domain initially has no vapors. Non-condensable gases are present, but they are quite insignificant. But because of the fuel's extremely high pressure, its impact was ignored. To reach a convergent solution, relaxation factors were modified. For spray atomization, select a density and temperature value that meet the necessary pressure requirements, the plenum is a non-reflective or wave transmitting boundary condition. No-slip adiabatic walls make up the remaining boundaries. The turbulent kinetic energy (ε) and specific dissipation rate (ω) are obtained from the output profile of internal flow simulation. The case setup for our study is described in Table 4.4.

**Table 4.4** Boundary conditions for nozzle flow and spray simulation

| Typeof Nozzle | Fuel | Internal nozzle flow condition (VOF + ZGB) | | | Chamber conditions for Spray simulation (DPM) | | |
|---|---|---|---|---|---|---|---|
| | | Inlet Pressure (MPa) | Outlet Pressure (MPa) | Turbulence Model | Density (kg/m$^3$) | Temp. (K) | Turbulence Model |
| ECN Spray C | n-Dodecane | 160 | 6 | k-ε (Standard) & k-ω (SST) | 22.8 | 303 | k-ε (Standard) & k-ω (SST) |

### 4.3.5 Validation for ECN spray-C results

In collaboration with the Engine Combustion Network (ECN), Payri et al. [109] conducted experimental investigations on an ECN spray fuel injector nozzle. Their focus was on determining the spray cone angle for n-dodecane fuel at an injection pressure of 1500 bar. Subsequently, in another study, Payri et al. [109] developed a cavitation induced Eulerian-Eulerian single-step method and implemented in the Open-FOAM for ECN spray C fuel injector. However, this method required grid refinement down to the sub-micron level to detect droplets without introducing discrete particles, making its application limited due to its high computational cost. In our current research; we introduced a novel methodology- the Eulerian-Lagrangian two-step approach. This method was implemented in the ANSYS-Fluent for ECN spray-C injector nozzle and cavitation coupled spray calculation has been obtained. Notably, this approach offers enhanced accuracy, and the results align more consistently with the experimental data on spray cone angles provided by ECN, as shown in Fig.4.25. The Eulerian-Eulerian single-step method fails to detect the exact boundary of the spray; it shows the diffusion of the fuel inside the spray domain. However present method shows clear boundary of the spray after image procession shown in Fig 4.25 (c). Moreover, calculation of spray is done by using file injection method which creates the exact condition for the cavitation assisted spray breakup. The developed spray patterns with proposed method exhibit a higher level of accuracy.

## 4.4 EXPERIMENTAL WORK FOR CAVITATION

These studies throw light on the cavitation phenomena inside nozzles, in particular on the identification of a pattern of quasi-steady-state cavitation flow. To observe cavitation in a nozzle, it must be transparent and capable to withstand high injection pressure and choking condition. A good-quality cavitation image will be convenient for the reader as well as for model validation. The purpose of this study is to determine the cavitation flow's characteristics. Three optical nozzles (CN 3, CN 4, and CN 5) were used to observe the cavitation flow. The fluid flows in a closed-circuit loop. The piston-type pump is used to feed fluid to the optical nozzle, and the fluid's outflow is collected in the reservoir. The bypass valve controls the flow rate and measures the corresponding pressure. Tables 4.5, 4.6, and 4.7 exhibit the operational and geometric observations for CN 3 in water, diesel, and WCO-based biodiesel, respectively. The CN 4 is employed to induce super cavitation on one side of the nozzle, and the results are shown in Table 4. 8.

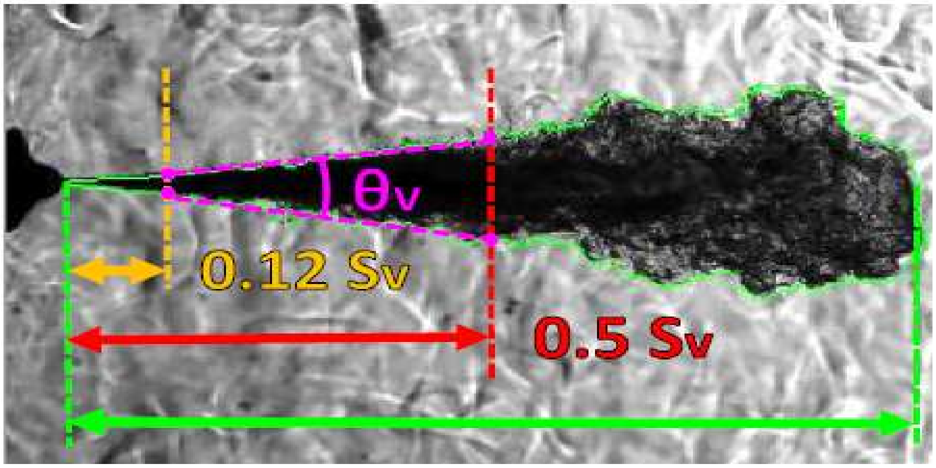

**(a) θ= 17.78°± 1.01° (**Experimental results of R. Payri et al. [109] & ECN)

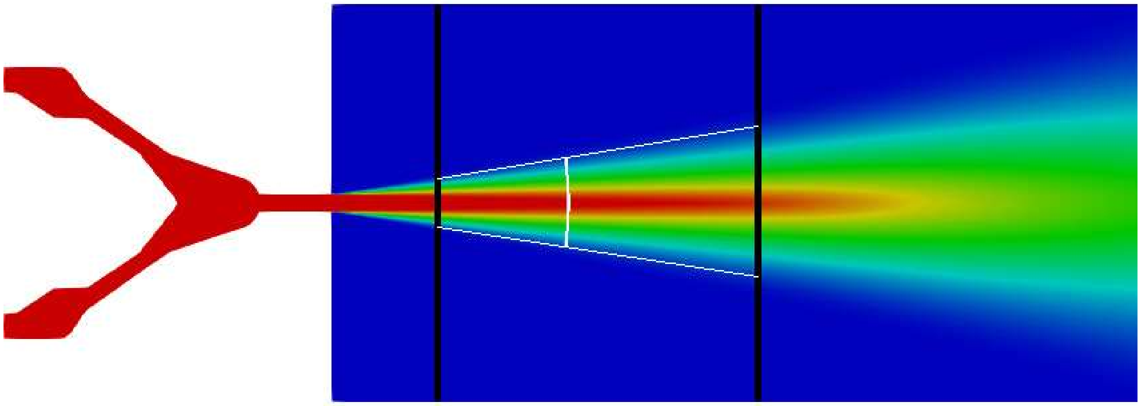

**(b) θ= 18.76°** (Single-step Coupled method R. Payri et al. [109])
(Calculated by using Eulerian-Eulerian coupling approach)

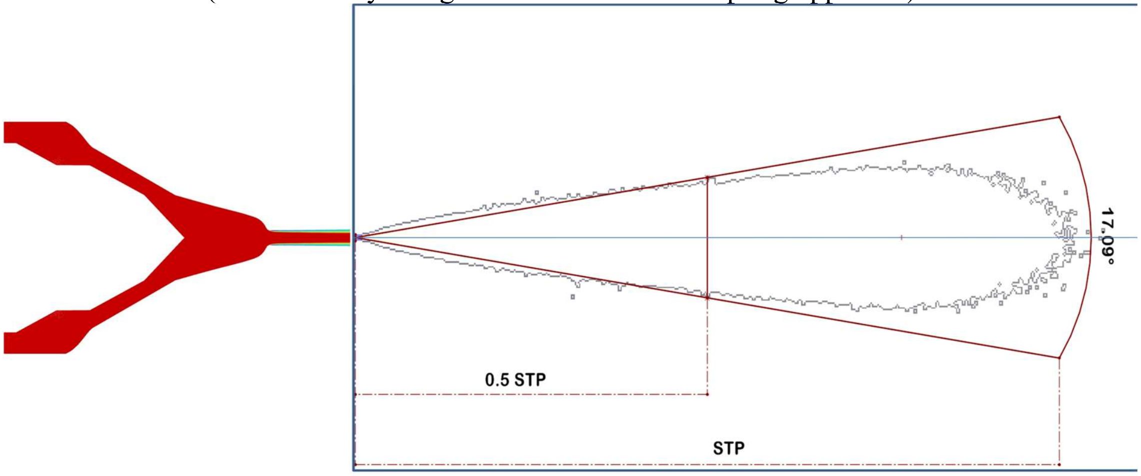

**(c) θ=17.09° (Two-step coupled method-Present Work**)
(Calculated by using Eulerian-Langrangian coupling approach)

**Fig 4.25** Comparison and validation of **Two-step coupled method** with experimental and numerical work of Payri et al. [109]

Finally, the cylindrical nozzle CN 5 was utilized to create a cavitation map with water, diesel, and WCO-biodiesel. The findings are presented in tables 4.9, 4.10, and 4.11. The results are then converted into non-dimensional parameters, such as the cavitation number, the discharge coefficient, and the Reynolds number.

### 4.4.1 Validation of experiment results

The experiment has been conducted with different injection pressures by operating a valve. As high-pressure water enters the nozzle, the water is accelerated, and the local pressure drops. When the local pressure falls below the vapour pressure, water begins to evaporate known as cavitation. The theoretical mass flow rate at a given pressure difference can be calculated using the following equation:

$$\dot{m}_{theo.} = \rho A V_{theo.} = \rho A \sqrt{2\Delta P/\rho} \qquad (4.1)$$

Fig. 4.26 compares the theoretical and actual mass flow rates determined at various injection pressures. The findings were obtained using two different nozzles (CN 3 and CN 5). The experiment yielded a lower mass flow rate than the theoretical findings. This is due to a decrease in the effective area caused by cavitation bubbles that form inside the nozzle. It is also worth noting that after 4 bar of injection pressure, the mass flow rate suddenly drops. This is related to the hydraulic flip phenomenon, in which air entrainment causes flow to detach from the nozzle's surface, resulting in annular flow.

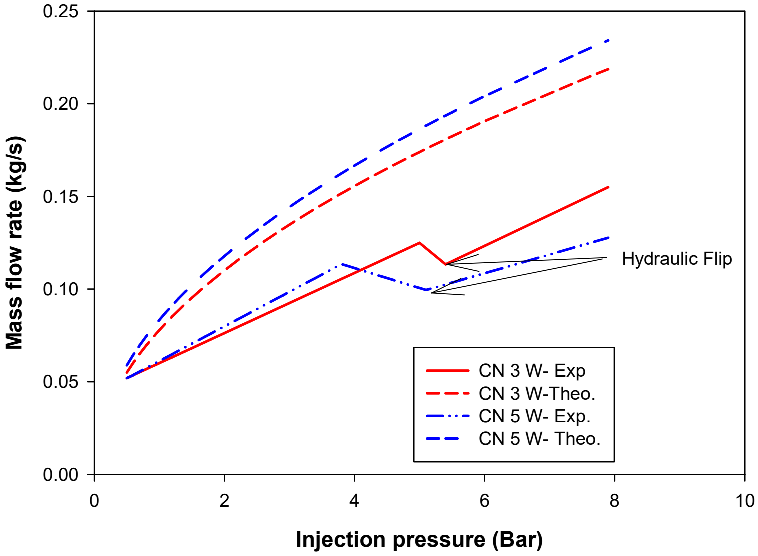

**Fig. 4.26** Comparison of theoretical and actual mass flow rate of water at different injection pressure.

### 4.4.2 Observation table

**Table 4.5** Observation table for cavitation nozzle-3 (CN 3W) using Water

| Sr No | Q (LPM) | Q (LPH) | Pressure (bar) | Length (m) | Width (m) | Depth (m) | L/W | Cross Section Area ($m^2$) | Hydro-dynamic mean Diameter (m) | Cavitation Stage |
|---|---|---|---|---|---|---|---|---|---|---|
| 1 | 3 | 180 | 0.7 | 0.02 | 0.005 | 0.001 | 4 | 0.000005 | 0.00167 | No Cavitation |
| 2 | 3.2 | 192 | 0.8 | 0.02 | 0.005 | 0.001 | 4 | 0.000005 | 0.00167 | No Cavitation |
| 3 | 3.6 | 216 | 1.2 | 0.02 | 0.005 | 0.001 | 4 | 0.000005 | 0.00167 | No Cavitation |
| 4 | 3.8 | 228 | 1.3 | 0.02 | 0.005 | 0.001 | 4 | 0.000005 | 0.00167 | No Cavitation |
| 5 | 4.2 | 252 | 1.5 | 0.02 | 0.005 | 0.001 | 4 | 0.000005 | 0.00167 | Inception |
| 6 | 4.6 | 276 | 1.8 | 0.02 | 0.005 | 0.001 | 4 | 0.000005 | 0.00167 | Inception |
| 7 | 4.8 | 288 | 2.1 | 0.02 | 0.005 | 0.001 | 4 | 0.000005 | 0.00167 | Inception |
| 8 | 5 | 300 | 2.2 | 0.02 | 0.005 | 0.001 | 4 | 0.000005 | 0.00167 | Growth |
| 9 | 5.5 | 330 | 2.6 | 0.02 | 0.005 | 0.001 | 4 | 0.000005 | 0.00167 | Growth |
| 10 | 5.75 | 345 | 3 | 0.02 | 0.005 | 0.001 | 4 | 0.000005 | 0.00167 | Growth |
| 11 | 6 | 360 | 3.3 | 0.02 | 0.005 | 0.001 | 4 | 0.000005 | 0.00167 | Growth |
| 12 | 6.25 | 375 | 3.9 | 0.02 | 0.005 | 0.001 | 4 | 0.000005 | 0.00167 | Growth |
| 13 | 6.5 | 390 | 4.1 | 0.02 | 0.005 | 0.001 | 4 | 0.000005 | 0.00167 | Super Cavitation |
| 14 | 6.75 | 405 | 4.3 | 0.02 | 0.005 | 0.001 | 4 | 0.000005 | 0.00167 | Super Cavitation |
| 15 | 7 | 420 | 4.5 | 0.02 | 0.005 | 0.001 | 4 | 0.000005 | 0.00167 | Super Cavitation |
| 16 | 7.25 | 435 | 5 | 0.02 | 0.005 | 0.001 | 4 | 0.000005 | 0.00167 | Super Cavitation |
| 17 | 6.8 | 408 | 5.4 | 0.02 | 0.005 | 0.001 | 4 | 0.000005 | 0.00167 | Hydraulic Flip |
| 18 | 7.2 | 432 | 5.8 | 0.02 | 0.005 | 0.001 | 4 | 0.000005 | 0.00167 | Hydraulic Flip |

**Table 4.6** Observation table for cavitation nozzle-3 (CN 3D) using Diesel

| Sr No | LPM Measured | LPM Actual | Pressure (bar) | Length (m) | Width (m) | Depth (m) | L/W | Cross Section Area ($m^2$) | Hydro-dynamic mean Diameter (m) | Cavitation Stage |
|---|---|---|---|---|---|---|---|---|---|---|
| 1 | 3 | 4.64 | 0.6 | 0.02 | 0.005 | 0.001 | 4 | 0.000005 | 0.00167 | No |
| 2 | 3.6 | 5.85 | 1 | 0.02 | 0.005 | 0.001 | 4 | 0.000005 | 0.00167 | No |
| 3 | 4 | 6.68 | 1.2 | 0.02 | 0.005 | 0.001 | 4 | 0.000005 | 0.00167 | No |
| 4 | 4.4 | 7.54 | 1.5 | 0.02 | 0.005 | 0.001 | 4 | 0.000005 | 0.00167 | No |
| 5 | 5 | 8.87 | 2 | 0.02 | 0.005 | 0.001 | 4 | 0.000005 | 0.00167 | No |
| 6 | 5.25 | 9.44 | 2.3 | 0.02 | 0.005 | 0.001 | 4 | 0.000005 | 0.00167 | Weak Inception |
| 7 | 5.8 | 10.72 | 2.7 | 0.02 | 0.005 | 0.001 | 4 | 0.000005 | 0.00167 | Strong Inception |
| 8 | 6 | 11.19 | 2.9 | 0.02 | 0.005 | 0.001 | 4 | 0.000005 | 0.00167 | Growth |
| 9 | 6.5 | 12.39 | 3 | 0.02 | 0.005 | 0.001 | 4 | 0.000005 | 0.00167 | Growth |
| 10 | 7 | 13.61 | 3.8 | 0.02 | 0.005 | 0.001 | 4 | 0.000005 | 0.00167 | Growth |
| 11 | 7.5 | 14.86 | 4.6 | 0.02 | 0.005 | 0.001 | 4 | 0.000005 | 0.00167 | Super Cavitation |
| 12 | 8 | 16.12 | 5.5 | 0.02 | 0.005 | 0.001 | 4 | 0.000005 | 0.00167 | Super Cavitation |

**Table 4.7** Observation table for cavitation nozzle-3 (CN 3B) using Bio-diesel

| Sr No | LPM | LPM Actual | Pressure (bar) | Length (m) | Width (m) | Depth (m) | L/W | Cross Section Area ($m^2$) | Hydro-dynamic mean Diameter (m) | Cavitation Stage |
|---|---|---|---|---|---|---|---|---|---|---|
| 1 | 4 | 6.68 | 0.57 | 0.02 | 0.005 | 0.001 | 4 | 0.000005 | 0.00167 | No |
| 2 | 4.6 | 7.98 | 0.87 | 0.02 | 0.005 | 0.001 | 4 | 0.000005 | 0.00167 | No Cavitation |
| 3 | 5 | 8.87 | 1.04 | 0.02 | 0.005 | 0.001 | 4 | 0.000005 | 0.00167 | No Cavitation |
| 4 | 5.5 | 10.02 | 1.34 | 0.02 | 0.005 | 0.001 | 4 | 0.000005 | 0.00167 | No Cavitation |
| 5 | 6.25 | 11.78 | 1.85 | 0.02 | 0.005 | 0.001 | 4 | 0.000005 | 0.00167 | No Cavitation |
| 6 | 6.75 | 12.99 | 2.13 | 0.02 | 0.005 | 0.001 | 4 | 0.000005 | 0.00167 | Inception |
| 7 | 6.75 | 12.99 | 2.26 | 0.02 | 0.005 | 0.001 | 4 | 0.000005 | 0.00167 | Inception |
| 8 | 7 | 13.61 | 2.32 | 0.02 | 0.005 | 0.001 | 4 | 0.000005 | 0.00167 | Growth |
| 9 | 7.25 | 14.23 | 2.58 | 0.02 | 0.005 | 0.001 | 4 | 0.000005 | 0.00167 | Super Cavitation |
| 10 | 8 | 16.12 | 4.74 | 0.02 | 0.005 | 0.001 | 4 | 0.000005 | 0.00167 | Hydraulic Flip |

**Table 4.8** Observation table for cavitation nozzle-4 (CN 4W) using Water

| Sr No | LPM | LPH | Pressure (bar) | Small Length (m) | Large Length (m) | Width (m) | Depth (m) | L/W (Small) | L/W (Large) | Cross Section Area ($m^2$) | Hydraulic Diameter (m) |
|---|---|---|---|---|---|---|---|---|---|---|---|
| 1 | 3 | 180 | 0.4 | 0.0153 | 0.0173 | 0.008 | 0.001 | 1.9125 | 2.1625 | 0.000008 | 0.00178 |
| 2 | 3.6 | 216 | 0.6 | 0.0153 | 0.0173 | 0.008 | 0.001 | 1.9125 | 2.1625 | 0.000008 | 0.00178 |
| 3 | 4.2 | 252 | 0.8 | 0.0153 | 0.0173 | 0.008 | 0.001 | 1.9125 | 2.1625 | 0.000008 | 0.00178 |
| 4 | 4.6 | 276 | 1 | 0.0153 | 0.0173 | 0.008 | 0.001 | 1.9125 | 2.1625 | 0.000008 | 0.00178 |
| 5 | 4.8 | 288 | 1.2 | 0.0153 | 0.0173 | 0.008 | 0.001 | 1.9125 | 2.1625 | 0.000008 | 0.00178 |
| 6 | 5 | 300 | 1.4 | 0.0153 | 0.0173 | 0.008 | 0.001 | 1.9125 | 2.1625 | 0.000008 | 0.00178 |
| 7 | 5.5 | 330 | 1.7 | 0.0153 | 0.0173 | 0.008 | 0.001 | 1.9125 | 2.1625 | 0.000008 | 0.00178 |
| 8 | 6 | 360 | 2 | 0.0153 | 0.0173 | 0.008 | 0.001 | 1.9125 | 2.1625 | 0.000008 | 0.00178 |
| 9 | 6.5 | 390 | 2.3 | 0.0153 | 0.0173 | 0.008 | 0.001 | 1.9125 | 2.1625 | 0.000008 | 0.00178 |
| 10 | 7 | 420 | 2.6 | 0.0153 | 0.0173 | 0.008 | 0.001 | 1.9125 | 2.1625 | 0.000008 | 0.00178 |
| 11 | 7.5 | 450 | 3.2 | 0.0153 | 0.0173 | 0.008 | 0.001 | 1.9125 | 2.1625 | 0.000008 | 0.00178 |
| 12 | 8 | 480 | 3.6 | 0.0153 | 0.0173 | 0.008 | 0.001 | 1.9125 | 2.1625 | 0.000008 | 0.00178 |
| 13 | 8.5 | 510 | 3.9 | 0.0153 | 0.0173 | 0.008 | 0.001 | 1.9125 | 2.1625 | 0.000008 | 0.00178 |
| 14 | 9 | 540 | 4.4 | 0.0153 | 0.0173 | 0.008 | 0.001 | 1.9125 | 2.1625 | 0.000008 | 0.00178 |
| 15 | 9.5 | 570 | 4.8 | 0.0153 | 0.0173 | 0.008 | 0.001 | 1.9125 | 2.1625 | 0.000008 | 0.00178 |
| 16 | 10 | 600 | 5.2 | 0.0153 | 0.0173 | 0.008 | 0.001 | 1.9125 | 2.1625 | 0.000008 | 0.00178 |
| 17 | 11 | 660 | 6 | 0.0153 | 0.0173 | 0.008 | 0.001 | 1.9125 | 2.1625 | 0.000008 | 0.00178 |
| 18 | 12 | 720 | 6.6 | 0.0153 | 0.0173 | 0.008 | 0.001 | 1.9125 | 2.1625 | 0.000008 | 0.00178 |
| 19 | 13 | 780 | 7.5 | 0.0153 | 0.0173 | 0.008 | 0.001 | 1.9125 | 2.1625 | 0.000008 | 0.00178 |
| 20 | 14 | 840 | 8 | 0.0153 | 0.0173 | 0.008 | 0.001 | 1.9125 | 2.1625 | 0.000008 | 0.00178 |
| 21 | 15 | 900 | 8.9 | 0.0153 | 0.0173 | 0.008 | 0.001 | 1.9125 | 2.1625 | 0.000008 | 0.00178 |
| 22 | 16 | 960 | 9.6 | 0.0153 | 0.0173 | 0.008 | 0.001 | 1.9125 | 2.1625 | 0.000008 | 0.00178 |

**Table 4.9** Observation table for cavitation nozzle-5 (CN 5W) using Water

| Sr No | LPM | LPH | Pressure (bar) | Length (m) | Diameter (m) | L/D | Cross Section Area ($m^2$) | Hydraulic Diameter (m) | Cavitation Stage |
|---|---|---|---|---|---|---|---|---|---|
| 1 | 3 | 180 | 0.7 | 0.02 | 0.0025 | 8 | 4.90874E-06 | 0.0025 | No |
| 2 | 3.2 | 192 | 0.9 | 0.02 | 0.0025 | 8 | 4.90874E-06 | 0.0025 | No |
| 3 | 3.4 | 204 | 0.95 | 0.02 | 0.0025 | 8 | 4.90874E-06 | 0.0025 | No |
| 4 | 3.7 | 222 | 1 | 0.02 | 0.0025 | 8 | 4.90874E-06 | 0.0025 | No |
| 5 | 3.8 | 228 | 1.1 | 0.02 | 0.0025 | 8 | 4.90874E-06 | 0.0025 | No |
| 6 | 4 | 240 | 1.2 | 0.02 | 0.0025 | 8 | 4.90874E-06 | 0.0025 | No |
| 7 | 4.2 | 252 | 1.3 | 0.02 | 0.0025 | 8 | 4.90874E-06 | 0.0025 | No |
| 8 | 4.4 | 264 | 1.5 | 0.02 | 0.0025 | 8 | 4.90874E-06 | 0.0025 | No |
| 9 | 4.8 | 288 | 1.7 | 0.02 | 0.0025 | 8 | 4.90874E-06 | 0.0025 | Weak Inception |
| 10 | 5 | 300 | 2 | 0.02 | 0.0025 | 8 | 4.90874E-06 | 0.0025 | Strong Inception |
| 11 | 5.25 | 315 | 2.3 | 0.02 | 0.0025 | 8 | 4.90874E-06 | 0.0025 | Growth |
| 12 | 5.5 | 330 | 2.5 | 0.02 | 0.0025 | 8 | 4.90874E-06 | 0.0025 | Supercavitation |
| 13 | 5.75 | 345 | 2.8 | 0.02 | 0.0025 | 8 | 4.90874E-06 | 0.0025 | Supercavitation |
| 14 | 6 | 360 | 3.1 | 0.02 | 0.0025 | 8 | 4.90874E-06 | 0.0025 | Supercavitation |
| 17 | 6.25 | 375 | 3.4 | 0.02 | 0.0025 | 8 | 4.90874E-06 | 0.0025 | Supercavitation |
| 18 | 6.5 | 390 | 3.8 | 0.02 | 0.0025 | 8 | 4.90874E-06 | 0.0025 | Supercavitation |
| 20 | 6.1 | 366 | 5.1 | 0.02 | 0.0025 | 8 | 4.90874E-06 | 0.0025 | Hydrualic Flip |
| 16 | 6.4 | 384 | 5.5 | 0.02 | 0.0025 | 8 | 4.90874E-06 | 0.0025 | Hydraulic Flip |
| 24 | 6.45 | 387 | 5.6 | 0.02 | 0.0025 | 8 | 4.90874E-06 | 0.0025 | Hydraulic Flip |
| 25 | 6.7 | 402 | 6 | 0.02 | 0.0025 | 8 | 4.90874E-06 | 0.0025 | Hydraulic Flip |
| 26 | 7.4 | 444 | 7.6 | 0.02 | 0.0025 | 8 | 4.90874E-06 | 0.0025 | Hydraulic Flip |
| 27 | 7.7 | 462 | 7.9 | 0.02 | 0.0025 | 8 | 4.90874E-06 | 0.0025 | Hydraulic Flip |

**Table 4.10** Observation table for cavitation nozzle-5 (CN 5D) using Diesel

| Sr. No. | LPM Measured | LPM (Calibrated) | Pressure (bar) | Length (m) | Diameter (m) | L/D | Cross Section Area ($m^2$) | Hydraulic Diameter (m) | Cavitation Stage |
|---|---|---|---|---|---|---|---|---|---|
| 1 | 3 | 3.29 | 0.6 | 0.02 | 0.0025 | 8 | 4.90874E-06 | 0.0025 | No |
| 2 | 3.4 | 3.73 | 0.7 | 0.02 | 0.0025 | 8 | 4.90874E-06 | 0.0025 | No |
| 3 | 4 | 4.39 | 1 | 0.02 | 0.0025 | 8 | 4.90874E-06 | 0.0025 | No |
| 4 | 4.6 | 5.04 | 1.3 | 0.02 | 0.0025 | 8 | 4.90874E-06 | 0.0025 | No |
| 5 | 5 | 5.48 | 1.6 | 0.02 | 0.0025 | 8 | 4.90874E-06 | 0.0025 | No |
| 6 | 5.5 | 6.03 | 1.8 | 0.02 | 0.0025 | 8 | 4.90874E-06 | 0.0025 | Weak Incepation |
| 7 | 6 | 6.58 | 2.3 | 0.02 | 0.0025 | 8 | 4.90874E-06 | 0.0025 | Strong Inception |
| 8 | 6.25 | 6.86 | 2.4 | 0.02 | 0.0025 | 8 | 4.90874E-06 | 0.0025 | Growth |
| 9 | 6.5 | 7.1346769 | 2.5 | 0.02 | 0.0025 | 8 | 4.90874E-06 | 0.0025 | Growth |
| 10 | 6.75 | 7.40 | 2.9 | 0.02 | 0.0025 | 8 | 4.90874E-06 | 0.0025 | Super Cavitation |
| 11 | 7 | 7.68 | 3.4 | 0.02 | 0.0025 | 8 | 4.90874E-06 | 0.0025 | Super Cavitation |
| 12 | 7.25 | 7.95 | 3.8 | 0.02 | 0.0025 | 8 | 4.90874E-06 | 0.0025 | Super Cavitation |
| 13 | 7.4 | 8.12 | 4.4 | 0.02 | 0.0025 | 8 | 4.90874E-06 | 0.0025 | Hydraulic Flip |
| 14 | 7.5 | 8.23 | 4.8 | 0.02 | 0.0025 | 8 | 4.90874E-06 | 0.0025 | Hydraulic Flip |
| 15 | 8 | 8.78 | 5.6 | 0.02 | 0.0025 | 8 | 4.90874E-06 | 0.0025 | Hydraulic Flip |

**Table 4.11** Observation table for cavitation nozzle-5 (CN 5D) using Bio-diesel

| Sr. No. | LPM Measured | LPM Actual | Pressure (bar) | Length (m) | Diameter (m) | L/D | Cross Section Area ($m^2$) | Hydro-dynamic mean Diameter (m) | Cavitation Stage |
|---|---|---|---|---|---|---|---|---|---|
| 1 | 3 | 3 | 0.5 | 0.02 | 0.0025 | 8 | 4.90874E-06 | 0.0025 | No Cavitation |
| 2 | 3.2 | 3.2 | 0.6 | 0.02 | 0.0025 | 8 | 4.90874E-06 | 0.0025 | No Cavitation |
| 3 | 3.8 | 3.8 | 0.8 | 0.02 | 0.0025 | 8 | 4.90874E-06 | 0.0025 | No Cavitation |
| 4 | 4.6 | 4.6 | 1.1 | 0.02 | 0.0025 | 8 | 4.90874E-06 | 0.0025 | No Cavitation |
| 5 | 5 | 5 | 1.4 | 0.02 | 0.0025 | 8 | 4.90874E-06 | 0.0025 | No Cavitation |
| 6 | 5.5 | 5.5 | 1.8 | 0.02 | 0.0025 | 8 | 4.90874E-06 | 0.0025 | No Cavitation |
| 7 | 6 | 6 | 2 | 0.02 | 0.0025 | 8 | 4.90874E-06 | 0.0025 | No Cavitation |
| 8 | 6.25 | 6.25 | 2.2 | 0.02 | 0.0025 | 8 | 4.90874E-06 | 0.0025 | Inception |
| 9 | 6.25 | 6.25 | 2.5 | 0.02 | 0.0025 | 8 | 4.90874E-06 | 0.0025 | Growth |
| 10 | 6.5 | 6.5 | 2.6 | 0.02 | 0.0025 | 8 | 4.90874E-06 | 0.0025 | Growth |
| 11 | 7 | 7 | 3.1 | 0.02 | 0.0025 | 8 | 4.90874E-06 | 0.0025 | Super Cavitation |
| 12 | 7.5 | 7.5 | 4.9 | 0.02 | 0.0025 | 8 | 4.90874E-06 | 0.0025 | Hydraulic Flip |
| 13 | 8 | 8 | 5.6 | 0.02 | 0.0025 | 8 | 4.90874E-06 | 0.0025 | Hydraulic Flip |

### 4.4.3 Uncertainty analysis

While measuring a quantity by using an instrument, the recorded value will always have a degree of uncertainty. This degree of uncertainty must be reflected in the derived quantity. The maximum possible uncertainty in performance parameters was estimated using the method proposed by Kline and McClintock. Uncertainty was calculated from the least count of the instrument output and the accuracy of the instrument. If the result (R) depends on independent variables (like $x_1$, x2,...xn), then the uncertainty or error in the value of 'R' is given by

$$\frac{\Delta R}{R} = \sqrt{\left[\left(\frac{\Delta x_1}{x_1}\right)^2 + \left(\frac{\Delta x_2}{x_2}\right)^2 + \cdots + \left(\frac{\Delta x_n}{x_n}\right)^2\right]} \tag{4.2}$$

Where $\left(\frac{\Delta x_1}{x_1}\right), \left(\frac{\Delta x_2}{x_2}\right)$are errors in independent variables.

In this investigation, flow rate and pressure are measured using a calibrated rotameter and pressure transmitter. The rotameter was calibrated using ISO 4185-1980 and had a measurement error of ±2% of full scale. The dimensions of the nozzle are measured using a 3D microscope with a minimum count of 0.1 micrometre. The dimension measurement error is estimated at ±1%. In this study, density, viscosity, and vapor pressure are considered standard fluid parameters. Based on these direct measured parameters, the following parameters were derived: (a) Reynolds number (b) cavitation number (c) discharge coefficient.

#### (a) Uncertainty in Reynolds number

Here is sample calculation of Reynolds Number Uncertainty:

The values of parameters and its error are given in Table 4.12.

**Table 4.12** The parameters used for Reynolds number

| | |
|---|---|
| $\rho = 1000, (kg/m^3)$ | $\delta\rho = 0$ |
| $v = 10.38, (m/s)$ | $\delta v = 1.67\%$ |
| $d = 4.167 \cdot 10^{-4}, (m)$ | $\delta d = 1\%$ |
| $\mu = 7.89 \cdot 10^{-4}, (Pa \cdot s)$ | $\delta\mu = 0$ |

Reynolds Number (Re):

$$Re = \frac{\rho v d}{\mu} = \frac{1000 * 10.38 * 4.167 * 10^{-4}}{7.89 * 10^{-4}} = 5482.06$$

Uncertainty in Reynolds Number (Re) is given by:

- $\delta Re = \sqrt{\left(\frac{\delta Re}{\partial \rho} * \delta\rho\right)^2 + \left(\frac{\delta Re}{\partial V} * \delta V\right)^2 + \left(\frac{\delta Re}{\partial d} * \delta d\right)^2 + \left(\frac{\delta Re}{\partial \mu} * \delta\mu\right)^2}$

$$\frac{\partial Re}{\partial \rho} = \frac{VD}{\mu} = \left(\frac{10.38 * 4.167 \cdot 10^{-4}}{7.89 \cdot 10^{-4}}\right) = 5.482 \ \ (kg^{-1}m^{3})$$

$$\frac{\partial Re}{\partial v} = \frac{\rho D}{\mu} = \left(\frac{1000 * 4.167 \cdot 10^{-4}}{7.89 \cdot 10^{-4}}\right) = 528.14 \ \ (kg\, m^{-2}s^{-1})$$

$$\frac{\partial Re}{\partial d} = \frac{\rho V}{\mu} = \left(\frac{1000 * 10.38}{7.89 \cdot 10^{-4}}\right) = 13155893.54 \ \ (kg\, m^{-1}s^{-1})$$

$$\frac{\partial Re}{\partial \rho} = -\frac{\rho VD}{\mu^{2}} = -\left(\frac{1000 * 10.38 * 4.167 \cdot 10^{-4}}{(7.89 \cdot 10^{-4})^{2}}\right) = -6948112.59 \ \ (kg\, m^{3}s^{-2}Pa^{-1})$$

$$\delta Re = \sqrt{(5.482 * 0)^{2} + \left(528.14 * \frac{1.67 * 10.38}{100}\right)^{2} + \left(13155893.54 * \frac{1 * 4.167 * 10^{-4}}{100}\right)^{2} + (-6948112.59 * 0)^{2}}$$

$$\delta Re = \sqrt{8381.58 + 3005.30} = 106.70$$

$$\delta Re \ = \frac{106.70}{5482.06} = 0.0195 = 1.95\%$$

$$\boxed{\boldsymbol{\delta Re = 1.95}\%}$$

**(b)Uncertainty in Cavitation number**

Values are considered to calculate cavitation number is given in Table 4.13.

**Table 4.13** The parameters used for Cavitation number

| | |
|---|---|
| $P_b = 101300, (Pa)$ | $\delta P_b = 0$ |
| $P_v = 4000, (Pa)$ | $\delta P_v = 0$ |
| $\rho = 1000, (kg/m^{3})$ | $\delta\rho = 0$ |
| $v = 10.38, (m/s)$ | $\delta v = 1.67\%$ |

Cavitation Number (CN):

$$CN = \frac{P_b - P_v}{\frac{1}{2}\rho v^{2}} = \frac{101300 - 4000}{\frac{1}{2} * 1000 * (10.38^{2})} = \frac{97300}{53872.2} = 1.80$$

Uncertainty in Cavitation Number (CN) is given by:

- ➢ $\delta CN = \sqrt{\left(\frac{\delta CN}{\partial P_b} * \delta P_b\right)^{2} + \left(\frac{\delta CN}{\partial P_v} * \delta P_v\right)^{2} + \left(\frac{\delta CN}{\partial \rho} * \delta\rho\right)^{2} + \left(\frac{\delta CN}{\partial v} * \delta v\right)^{2}}$

$$\frac{\partial CN}{\partial P_b} = \frac{1}{\frac{1}{2}\rho v^{2}} = \left(\frac{1}{\frac{1}{2} * 1000 * 10.38^{2}}\right) = 1.86 \cdot 10^{-5}\, , (kg^{-1}m^{1}s^{2})$$

$$\frac{\partial CN}{\partial P_v} = -\frac{1}{\frac{1}{2}\rho v^{2}} = -\left(\frac{1}{\frac{1}{2} * 1000 * 10.38^{2}}\right) = -1.86 \cdot 10^{-5}\, , (kg^{-1}m^{1}s^{2})$$

$$\frac{\partial CN}{\partial P_b} = -\frac{(P_b - P_v)}{\frac{1}{2}\rho^2 v^2} = -\left(\frac{101300 - 4000}{\frac{1}{2} * 1000^2 * 10.38^2}\right) = -1.806 \cdot 10^{-3}, (kg^{-1}m^3)$$

$$\frac{\partial CN}{\partial v} = -\frac{(P_b - P_v) * 2 * v}{\frac{1}{2}\rho v^3} = -\left(\frac{(101300 - 4000) * 2 * 10.38}{\frac{1}{2} * 1000 * 10.38^3}\right) = -0.361\ , (m^{-1}s^1)$$

$$\delta CN$$

$$= \sqrt{(1.86 \cdot 10^{-5} * 0)^2 + (-1.86 \cdot 10^{-5} * 0)^2 + (-1.806 \cdot 10^{-3} * 0)^2 + \left(-0.361 * \frac{10.38 * 1.67}{100}\right)^2}$$

$$\delta CN = \sqrt{0.003916} = 0.06258$$

$$\delta CN = \frac{0.06258}{1.8} = 0.03477$$

$$\boxed{\boldsymbol{\delta CN = 3.477}\ \%}$$

**(b) Uncertainty in Discharge co-efficient**

Values are considered to calculate discharge coefficient is given in Table 4.14.

**Table 4.14** The parameters used for discharge coefficient

| | |
|---|---|
| $Q = 5.194 \cdot 10^{-5}, (m^3/s)$ | $\delta Q = 1.67\%$ |
| $A = 5 \cdot 10^{-6}, (m^2)$ | $\delta A = 0$ |
| $v = 12.456, (m/s)$ | $\delta v = 1.67\%$ |

Co-efficient of Discharge ($C_d$):

$$C_d = \frac{Q}{Av} = \frac{5.194 * 10^{-5}}{5 * 10^{-6} * 12.456} = 0.834$$

Uncertainty in Cavitation Number (CN) is given by:

$$\delta C_d = \sqrt{\left(\frac{\delta C_d}{\partial Q} * \delta Q\right)^2 + \left(\frac{\delta C_d}{\partial A} * \delta A\right)^2 + \left(\frac{\delta C_d}{\partial v} * \delta v\right)^2}$$

$$\frac{\partial C_d}{\partial Q} = \frac{1}{Av} = \left(\frac{1}{5 * 10^{-6} * 12.456}\right) = 16056.52\ ,$$

$$\frac{\partial C_d}{\partial A} = -\frac{Q}{A^2 v} = -\left(\frac{5.194 * 10^{-5}}{(5 * 10^{-6})^2 * 12.456}\right) = -833975.6\ ,$$

$$\frac{\partial C_d}{\partial A} = -\frac{Q}{Av^2} = -\left(\frac{5.194 * 10^{-5}}{5 * 10^{-6} * 12.456^2}\right) = -0.067\ , ()$$

$$\delta C_d$$

$$= \sqrt{\left(16056.52 * \frac{5.194 * 10^{-5} * 1.67}{100}\right)^2 + (-833975.6 * 0)^2 + \left(-0.067 * \frac{12.456 * 1.67}{100}\right)^2}$$

$$\delta C_d = \sqrt{0.000194 + 0.000194}$$

$$\delta C_d = \frac{0.0197}{0.834} = 0.0236$$

$$\boxed{\boldsymbol{\delta C_d = 2.36\%}}$$

Finally, the uncertainty of the different parameters and non-dimensional numbers are summarized in Table 4.15.

**Table 4.15** Accuracy of Measurements and Uncertainty of the calculated results

| Measurement | Instrument | Error/Uncertainty |
|---|---|---|
| Volume flow rate | Rotameter | ± 2% |
| Diameter | 3D microscope | ± 1% |
| Pressure | Pressure transmitter | ± 1% |
| Velocity | - | ± 2% |
| Reynolds number | - | ± 1.95 % |
| Cavitation number | - | ± 3.477% |
| Discharge co-efficient | - | ± 2.36% |

## 4.5 EXPERIMENTAL WORK FOR SPRAY

The experiment used a Delphi single-hole injector with a 0.2 mm nozzle to determine macroscopic spray characteristics, such as (a) spray tip penetration (STP), (b) spray cone angle (SCA), and (c) spray area and volume. The spray tip penetration measures the distance between the nozzle tip and the spray tip. The spray cone angle is the angle of the spray boundary at half the distance of spray tip penetration. The region contained by the spray boundary corresponds to the spray area depicted in Fig. 4.27.

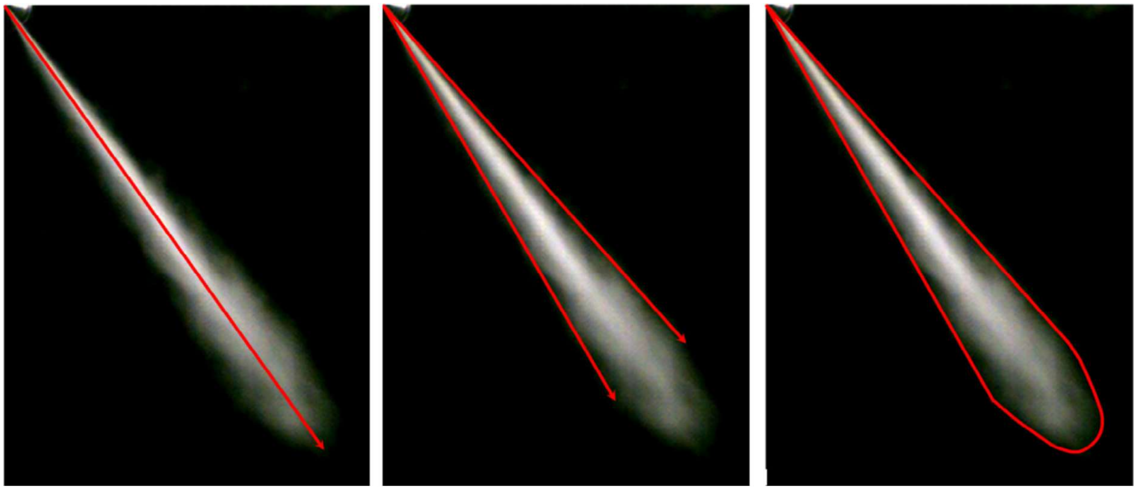

**Fig. 4.27** Macroscopic spray characteristics (a) spray tip penetration (b) spray cone angle (c) spray area [111]

### 4.5.1 Validation of Spray tip penetration (STP)

The formation of spray was captured using high-speed video recording via camera (1000 FPS). The recorded footage was imported into an image processing application. The single fuel injection event has been extracted from the film, and the start of injection (SOI) and end of injection (EOI) have been noted. The single injection video was subsequently processed for slow motion up to 100 times. The still image of spray development was collected at various time intervals. The raw image was then processed with an image processing tool in MATLAB using the Otsu method. The penetration length of the fuel spray as a function of time after injection begins is determined using processed pictures, as illustrated in Fig. 4.28.

**Fig 4.28** Development of spray after start of injection (SOI)

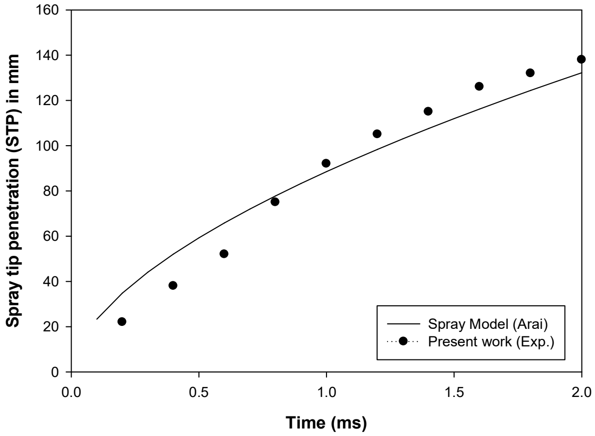

**Fig. 4.29** Comparison of STP with empirical model

The spray tip penetration was compared to the analytical model developed by Arai et al. [112] shown in Fig. 4.29. The results obtained in present experimentation are consistence with the empirical model.

### 4.6 WCO BIO-DIESEL PRODUCTION

It has been decided to develop an in-house biodiesel production unit that will function on the principle of hydrodynamic cavitation. As described in the previous chapter, waste cooking oil has been utilized to produce biodiesel since it is inexpensive and easily available in the local market. The transesterification process was carried out utilizing a cavitation reactor.

#### 4.6.1 Cavitation reactor

The production of biodiesel is dependent on the proper selection of cavitation reactor. The efficient reactor accelerates the reaction process and yields high-quality biodiesel. In this study, three different sizes of orifice-based cavitation reactors were investigated, as illustrated in Fig. 4.30. Initially, water is used to test the performance of the reactor. Each reactor's temperature rise over time (25 minutes) is calculated, and the best reactor is determined based on the data. The temperature of the fluid increases due to the collapse of cavitation bubbles, higher temperature rise indicates more intensity of cavitation. The temperature rise with orifice 3 is higher than that of orifice1 and orifice 2 shown in Fig. 4.31

#### 4.6.2 Biodiesel production Process

(1) Transesterification Process:

In this study, biodiesel was produced from used cooking oil using a hydrodynamic cavitation-based transesterification process. The reaction was carried out in an in-house biodiesel production setup, which included a cavitation reactor, a mixing tank, and a separation unit. The feedstock, used cooking oil (UCO), was first preheated to approximately 60°C to reduce its viscosity and enhance the reaction efficiency. A methanol-to-oil molar ratio of 6:1 was maintained throughout the process, with potassium hydroxide (KOH) as a catalyst at a concentration of 1% by weight of oil. The methanol and catalyst were premixed before being introduced into the reactor. The transesterification reaction was conducted under continuous cavitation conditions, ensuring efficient mixing and mass transfer. Samples were collected at 10-minute intervals to monitor the progression of the reaction. It was observed that after 30 minutes, the biodiesel yield reached its maximum, ranging between 85-90%. Beyond this point, no significant increase in yield was observed, indicating the completion of the transesterification reaction. The reaction was then stopped, and the mixture was transferred to the separation unit for the next stage.

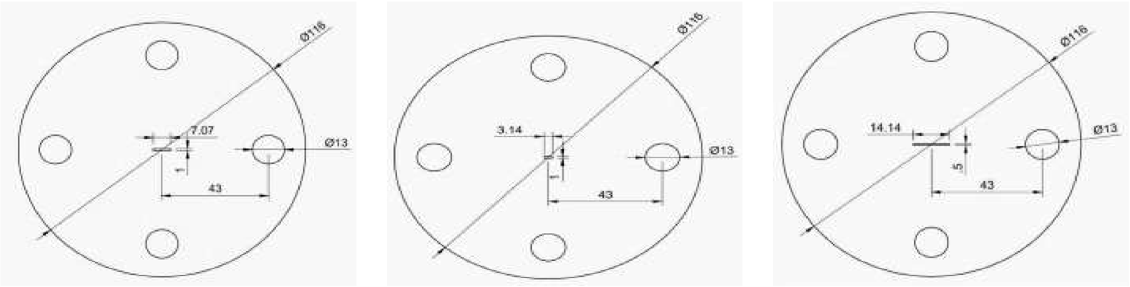

Orifice 1 (7.07 mm x 1 mm) Orifice 2 (3.14 mm x 1 mm) Orifice 3 (14.14 mm x 0.5 mm)

**Fig. 4.30** Orifice plates with different slit cross section

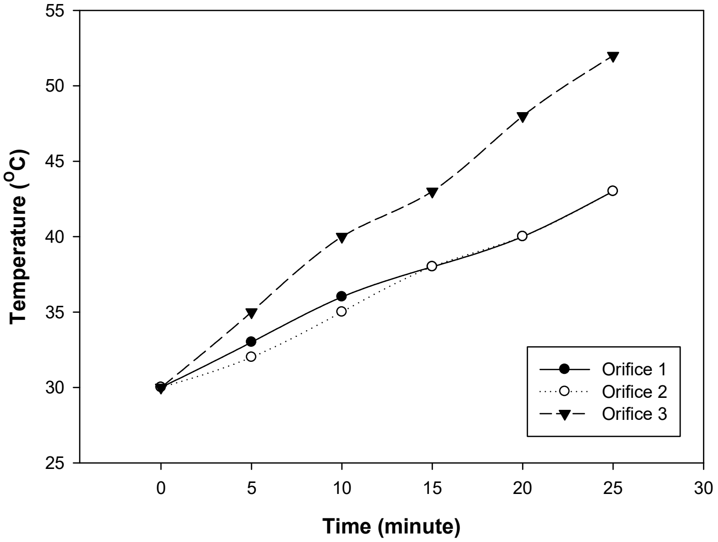

**Fig 4.31** Temperature rise with respect to time for different orifice

(2) Separation Process:

Following the transesterification reaction, the reaction mixture was allowed to settle under gravity separation conditions. Due to the difference in densities between biodiesel and glycerol, a clear phase separation was observed within 5 minutes. The heavier glycerol layer settled at the bottom, while the lighter biodiesel layer remained on top. The separated glycerol was carefully removed from the bottom, leaving behind the crude biodiesel. The efficiency of the separation process was visually confirmed, as the biodiesel layer appeared clear with minimal suspended impurities. This step ensured the effective removal of glycerol, which, if left unseparated, could negatively impact the quality of the final biodiesel product.

Fig. 4.32 depicts the sample collected every 5 minutes during a given period. Fig. 4.33 depicts the percentage yield for each time frame. More than 80% biodiesel production was produced after 25 minutes of reaction time. The maximum yield of 90% was reached after 40 minutes of reaction time.

**Fig. 4.32** Sample collected at every five minutes of time interval

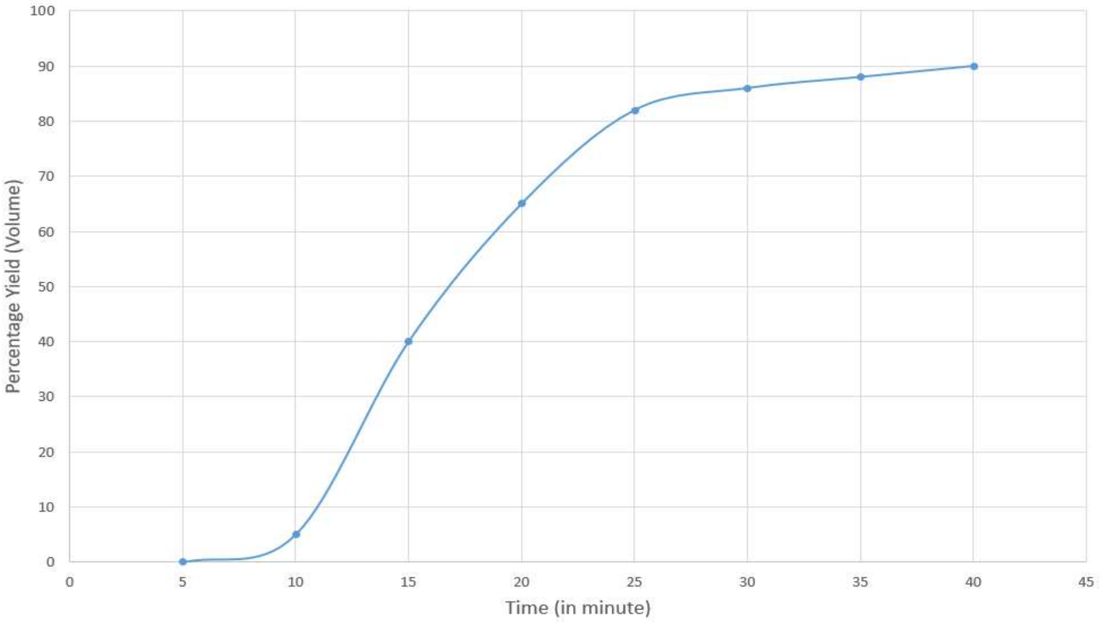

**Fig. 4.33** Percentage yield conversion with respect to time

(3) Washing Process:

To remove residual soap, catalyst, and excess methanol, the crude biodiesel underwent a washing process. Warm distilled water (50-60°C) was gently introduced into the biodiesel phase in a 1:1 volume ratio, and the mixture was stirred lightly to prevent excessive emulsification. The water was then allowed to settle for 10-15 minutes, after which it was drained from the bottom. This washing process was repeated two to three times until the wash water became clear, indicating the removal of impurities. The washing process was crucial in improving the purity of the biodiesel, as any residual catalysts and soaps could affect the fuel properties. Proper care was taken to avoid excessive agitation, which could lead to emulsion formation and prolonged separation times.

(4) Heating Process:

After washing, the biodiesel was subjected to a heating process to remove any residual water and moisture. The biodiesel was heated to a temperature of 110-120°C and maintained for 15-20 minutes to ensure complete moisture evaporation. This step was essential in preventing microbial growth, corrosion, and performance issues in diesel engines. Once the heating process was completed, the final dry biodiesel was allowed to cool to room temperature before being stored for further characterization and use. The removal of moisture was confirmed by the absence of water droplets or haze in the biodiesel.

**Fig 4.34** Waste cooking oil to Bio-diesel

This optimized process resulted in a high-quality biodiesel product with enhanced yield and purity. The combination of hydrodynamic cavitation, efficient separation, washing, and moisture removal ensured the production of biodiesel that met standard fuel quality specifications.